MANUSCRIPT

Preliminary assessment of the design requirement against blast load for ship superstructure

L. Liu[a], P.J. Tan[a*], Y. Yuan[b] and P. Wrobel[a]

[a] Department of Mechanical Engineering, University College London, London WC1E 7JE, UK
[b] Department of Mechanical Engineering, Imperial College London, London SW7 2AZ, UK

ARTICLE HISTORY
Compiled June 3, 2019

ABSTRACT

This paper attempts to rationalise, and assess, the existing design requirement for the sizing of the outer plating of a ship superstructure against an external air blast. First, a review of the current design guideline, specifically on how the blast load parameters were specified by the Rules and Regulations of Lloyd's Register and the assumptions behind the use of the scantling equation, is provided by way of a design case study. Next, a non-linear SDOF model that incorporates a new plastic membrane phase is developed in this paper, together with three-dimensional FE simulations, to model the large inelastic deformation of the platings. The required plate thickness needed to resist a specified load intensity is then compared for the three different methods, viz. Lloyd's Register design rule, SDOF and FE. As expected, it will be shown that existing design guideline achieves the purpose of maintaining water or gas-tight integrity of a plating; however, there exists significant unnecessary redundancies (or over-design) with implications on light-weighting. Additionally, the results will be summarised in the form of a failure map that will be useful to designers.

KEYWORDS
navy ship superstructure outer plating; external blast; rules and regulations; single degree of freedom (SDOF); finite elements modelling (FE)

---

*Corresponding Author. Email: pj.tan@ucl.ac.uk

Nomenclature

B	superstructure width
E	Young's modulus
D	flexural rigidity of the plate per unit length, $Eh^3/(12(1-\nu^2))$
H	superstructure height
H_s	standard superstructure height, taken as 2.3 m
I^*	dimensionless impulsive loading intensity,$V_0/\sqrt{\sigma_0/\rho}$
K_l	load factor of SDOF
K_m	mass factor of SDOF
L	superstructure length
M	total mass of plae
M_E	equivalent mass of SDOF
P	pressure of blast wave
P_0	atmospheric pressure taken as 101.3 KP_a
P_i	peak incident overpressure
P_i^-	negative peak incident overpressure
P_r	peak reflected overpressure
P_r^-	negative peak reflected overpressure
P_s	stagnation pressure
R_e	maximum elastic resistance of plate
R_u	ultimate resistance of plate
R_{up}	partial failure resistance
U_0	speed of sound in air, taken as 340 m/s
V_0	initial velocity
W	the weight of explosive(in TNT-equivalent)
Z	scaled distance, $Z = r/W^{1/3}$
a	length of plate
b	width of plate
d_c	characteristic dimension of ship superstructure
f_{DLF}	dynamic loading factor
f_b	blast wave parameter
f_γ	plate aspect ratio factor
f_σ	stress factor
h	plate thickness
k	spring constant of plate
k_E	equivalent spring constant of SDOF
m_0	unit plastic moment, $m_0 = \sigma_0 h^2/4$
n_0	unit membrane force, $n_0 = \sigma_0 h$
r	standoff distance
t	time
t_0	standard loading duration, taken as 0.4 s
t_a	arrival time
t_n	natural period
t_p^+	positive overpressure duration
t_p^-	negative overpressure duration
t_s	stagnation time
q	pressure on unit area of the plate
γ	aspect ratio of plate, a/b

ε	tensile strain
ε_{max}	maximum tensile strain on the plate
ε_{rup}	rupture strain
ε^p	equivalent plastic strain (PEEQ)
ν	Poisson's ratio
ρ	density of material
σ_0	static yield stress
σ_d	dynamic yield stress
$\phi(x, y)$	shape function of plate
$\omega(x, y)$	deform function of plate
ω_c	magnitude of central deflection
ω_{ce}	central deflection for the maximum elastic resistance
ω_{cmax}	maximum central deflection
ω_{cu}	central deflection for the ultimate resistance
ω_{cup}	central deflection for partial failure

1. Introduction

Naval ships must be designed to resist various military loads – one example is external blast. In contrast to a near-field explosion which is characterised by high over-pressure and short loading duration, an external blast event is a massive far-field explosion in air with relatively lower over-pressure but longer loading duration. An external blast can be generated from a variety of threats including large quantities of conventional explosives and nuclear weapons, and the radius of the blast wave front is much larger than the longitudinal dimension of a typical naval ship as shown schematically in Fig. 1. As observed in full-scale military tests, a ship's superstructure[1] is more vulnerable compared to its hull because its outer platings [2] are usually designed only for water or gas-tight integrity, and its thickness has been minimised to reduce topside weight.

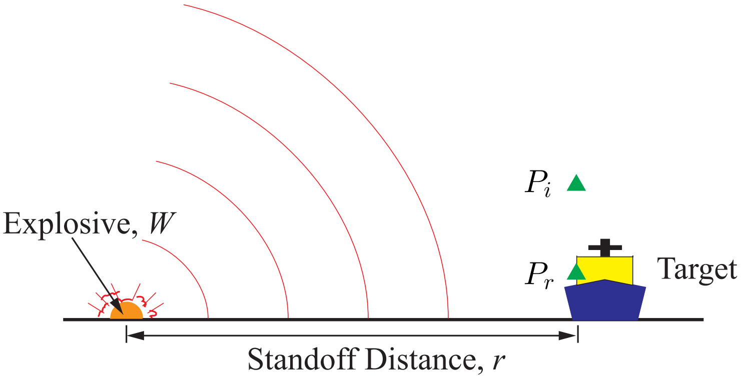

Figure 1. Schematic of an external blast environment.

Whilst there is a large body of literature on the response of structures to blast loading, there are relatively few – two exceptions are Dye and Lankford (1966) and Dow (1994) – that deals with the design of ship superstructures, with most focusing on either the design of individual stiffeners or the overall dynamic structural response. Notwithstanding, many classification societies – Registro Italiano Navale (2011), Germanischer Lloyd (2012), Lloyd's Register (2014), to name a few – have proposed various design guidelines against an external blast event. A major drawback, however, is that these design criteria were based on an elastic limit state, ignoring the fact that a ship plating, made of high-strength structural steel, could undergo significant plastic deformation, i.e. they can absorb a significant amount of energy when deforming in the plastic phase, before failure by material rupture.

Plating failure[3] is said to occur when the deformation exceeds a design limit state. In practice, a rectangular plate is typically supported along a fixed (or fully-clamped) boundary, and the blast may be assumed to impinge uniformly and normally on the

---

[1] The definition of 'ship superstructure' includes all the box-like structures above the main deck of a ship, and the term 'superstructure' covers the traditional meaning of 'superstructure' and 'deckhouse', as well as other unconventional structures, such as carrier hangar.

[2] The terms 'plating' and 'plate' are used interchangeably in accordance with the standard practice of shipbuilding industry.

[3] The terms 'failure' and 'damage' are often used interchangeably in the literature. In this paper, 'failure' shall refer to observable deformation such as incipient tearing of the plating from its boundary; whilst 'damage' is used to describe the degradation of stiffness of the elements used in the FE model.

plate. In such circumstances, the plate can develop a variety of mode shapes that changes with central deflection. Olson et al. (1993) introduced three different modes of plate deformation as follows: mode I: large inelastic deformation; mode II: tearing (material rupture) of the outer fibres along the support; mode III: transverse shear failure at the support. A similar categorisation can be extended to rectangular plates exposed to more general, non-impulsive blast conditions since they, too, exhibits similar large plastic deformation and progressive tearing along its boundary (US Navy 1990). Lloyd's Register (2014) stipulates that the outer plating of a ship superstructure must maintain its water and gas-tight function in an external blast. Incipient tearing of a plating - this always occurs at the mid-length of its longer edge along its boundary - typically occurs at a much lower blast impulse compared to transverse shear failure (mode III); hence, it is convenient to neglect the effects of transverse shear in this study. Therefore, a mode II response is employed as the limiting condition (or the design limit state) in the present study.

The Rules and Regulations for the Classification of Naval Ships by Lloyd's Register (2014), hereinafter referred to as LRN for brevity, provide design equations against external blast. However, their origin and the safety factor that was built into the scantling equation is unknown. It also worth noting that existing single degree of freedom (SDOF) models (US Army Corps of Engineers 1957a; Biggs 1964; US Navy 1990; Morison 2006) were formulated for civil engineering problems, and transformation factors were only provided for plates with aspect ratio between 1.0 to 2.0; by contrast, aspect ratios of up to 4.0 are often encountered in the platings of a ship superstructure. Moreover, steels used in ship construction are highly ductile and none of the previous SDOF models have considered this. In addition, existing FE models by Olson et al. (1993); Fagnan (1996); Yuan and Tan (2013); Yuan et al. (2016, 2017) simulate laboratory-scale platings; whether their predictions can be scaled-up for use in the design of ship platings between 0.5-3.0 m in length would need to be assessed. Unlike Yuan et al. (2016), the present paper focuses on rectangular plates and the development of a new 4-phases SDOF model to account for the energy absorbed by the significant membrane force that develops during large plastic deformation - it provides a direct means to determine incipient plate rupture.

This paper aims to elucidate, rationalise and assess the accuracy of the design guidelines by LRN; and, to develop non-linear single degree of freedom and finite element models as alternative approaches for predicting the minimum plating thickness needed to maintain water or gas-tight integrity of a ship superstructure. It is organised as follows: Section 2 reviews the design guidelines by LRN, focusing on the specification of blast loading parameters and the assumptions behind the scantling equation; a new SDOF model is developed in Section 3 that incorporates a plastic membrane phase; and three-dimensional FE models are developed in Section 4; Section 5 explains how the aforementioned models can be used to design the ship platings; and, Section 6 assesses the accuracy of LRN design procedure by comparing the predicted thicknesses using different methods, and the results are summarised in a failure map.

2. Rules and Regulations of Lloyd's Register: Designing against external blasts

2.1. Definition of parameters and scantling equation

A superstructure may be regarded as a rectangular box-like structure with length L, width B and height H, shown schematic in Fig. 2a. The incoming blast wave interacts with one of its vertical facets, known as the Front side, and this is where a superstructure experiences the highest overpressure as a blast wave propagates through it. Nearly all ship superstructures are constructed by transverse framing (Dow 1994), as opposed to an Isherwood system, where the platings are welded to their underlying primary structures such as frames and girders – see Fig. 2b. On this basis, the outer plating of a superstructure can be analysed as a monolithic plate with fully fixed boundaries, which greatly simplifies the problem (Det Norske Veritas 2010). A schematic of a fully clamped plate with dimensions a, b and h is shown in Fig. 2c. Note that its aspect ratio is defined as the ratio of its length to width given by $\gamma \triangleq a/b$. Here, a is the length of the plate so $\gamma \geq 1.0$.

The intensity of the external blast is denoted by the incident overpressure P_i, which is the peak side-on overpressure shown in Fig. 1. Another critical parameter is the duration of the positive overpressure phase t_p^+, this corresponds to the time at the end of the positive loading phase, beyond which the loading pressure is set to be zero even though, in reality, there follows a negative suction phase. LRN stipulates that P_i and t_p^+ are to be read from Fig. 3 if they were not specified in the design requirements.

It must be emphasised that the actual loading on the front face comes not only from the blast wave but also through interactions between the blast wave and the superstructure. By assuming a rigid superstructure, the peak reflected overpressure P_r can be written as (Dow 1994)

$$P_r = P_i(7P_0 + 4P_i)/(7P_0 + P_i), \tag{1}$$

where P_0 is the atmospheric pressure. The reflected overpressure (loading) curve is often represented as a bilinear curve, in which two lines intersect at the stagnation point. The pressure acting of the superstructure is assumed to diminish linearly until it reaches the stagnation pressure P_s. The value of stagnation pressure is given by

$$P_s = 3.5P_i(2P_0 + P_i)/(7P_0 + P_i), \tag{2}$$

and the time t_s to reach this point is

$$t_s = 3d_c/(U_0\sqrt{7P_0 + P_i}), \tag{3}$$

where d_c is a characteristic dimension (the smaller of either height H or half length $L/2$), U_0 is the speed of sound in air at 340 m/s. Hence, the reflected overpressure (loading) curve is characterised by four independent parameters P_r, P_s, t_s and t_p^+, see Fig. 4.

LRN uses a SDOF approach to calculate the dynamic response of the superstructure plating. A dynamic load factor f_{DLF} is introduced that accounts for the dynamic interactions between the blast load and plating. Its value is determined by the loading

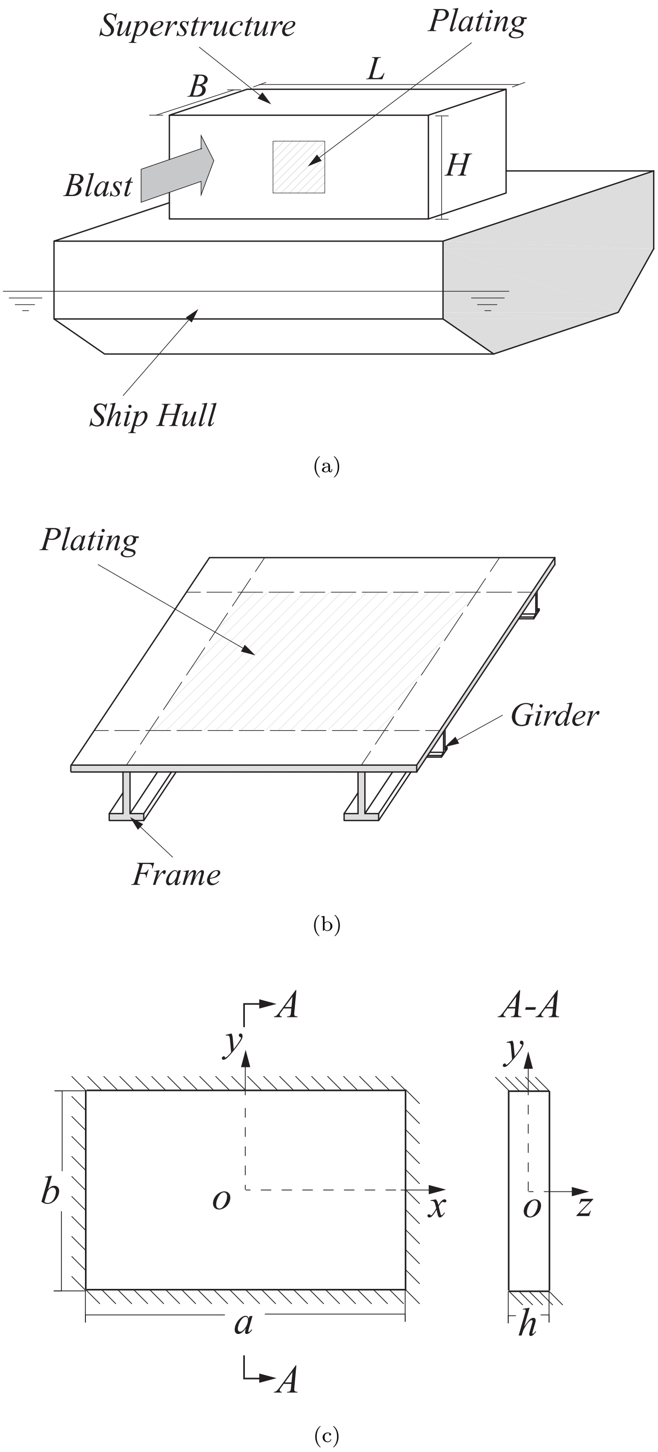

Figure 2. Schematic of a ship superstructure and its simplifications (adopted from Lloyd's Register (2014)): (a) Front face of a ship superstructure. The superstructure has length L, width B and height H; (b) A single plating is welded to its underlying primary structure, such as frames and girders; (c) Schematic of a fully clamped plate with length a, width b and thickness h where its aspect ratio is defined as $\gamma = a/b \geq 1.0$.

duration t_1 and the natural period of the plating t_n. The bilinear pressure loading is assumed to have an identical dynamic effect as a linearly-decreasing pulse which is rep-

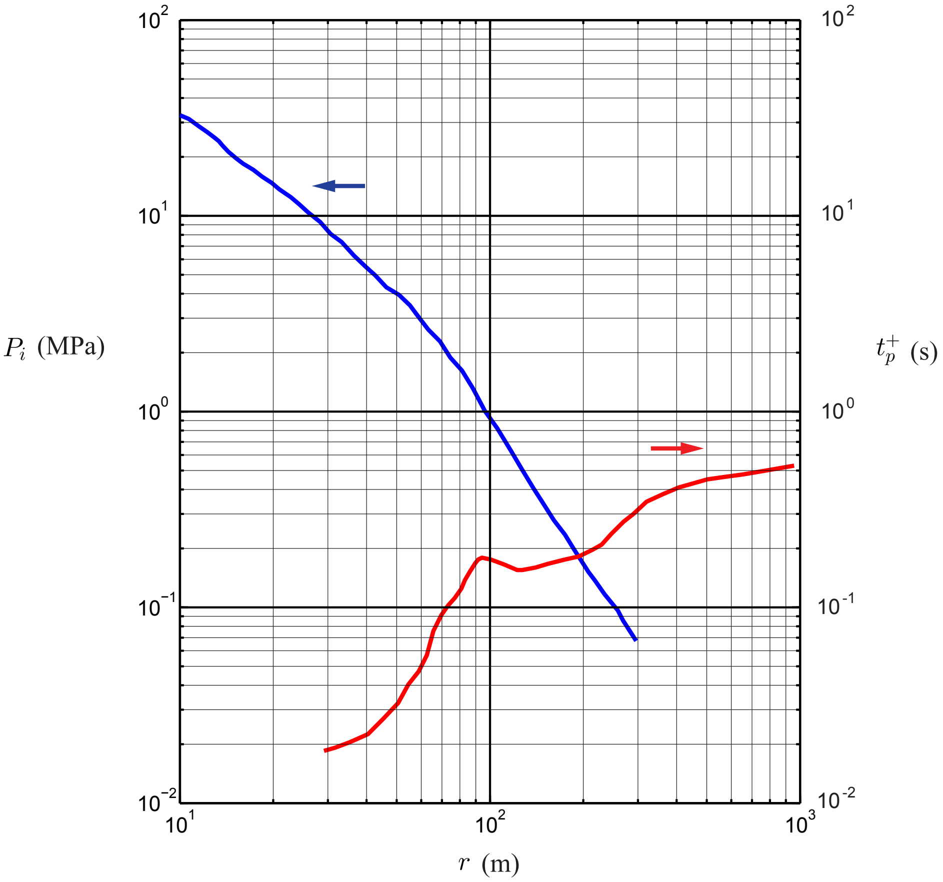

Figure 3. Blast parameters for 1 kilotonne of TNT (adapted from (Lloyd's Register 2014)).

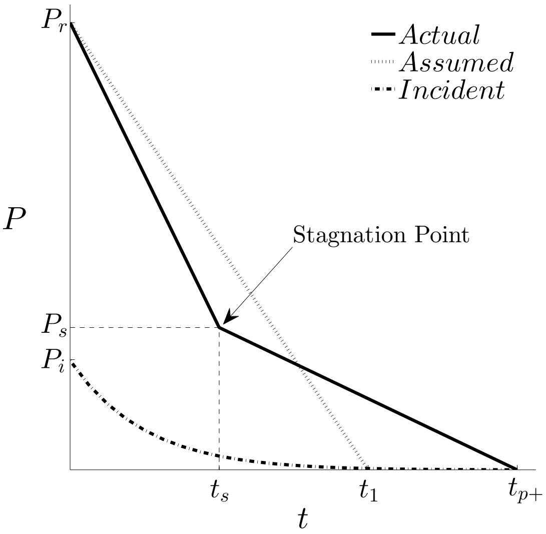

Figure 4. Schematic of pressure-time histories (adapted from Lloyd's Register (2014)). Solid line (—) gives the reflected overpressure on the front face of the superstructure; dash-dot (-·-) line is the incident overpressure (side-on overpressure) which decreases exponentially with time; dotted line (···) is the assumed pressure loading used to determine the dynamic load factor.

resented by a dotted line $(\cdots)$ in Fig. 4, and the loading duration t_1 is given by (Lloyd's Register 2014)

$$t_1 = P_r t_s / P_s. \tag{4}$$

Given a plating of length a, aspect ratio γ and thickness h, its natural period t_n is calculated through an empirical equation as follows (Lloyd's Register 2014):

$$t_n = \frac{1}{5537} \frac{a^2}{h\sqrt{\gamma^4 + 0.6045\gamma^2 + 1}}. \tag{5}$$

Then, the value of dynamic load factor f_{DLF} is obtained from Fig. 5 (Lloyd's Register 2014) after the ratio of the loading duration t_1 to the natural period of the plating t_n is found.

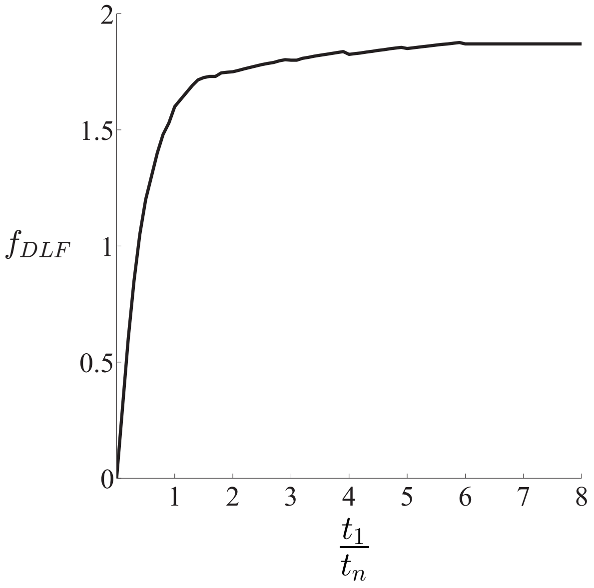

Figure 5. Empirical curve for the dynamic load factor f_{DLF} versus ratio of loading duration t_1 to the natural period of the plating t_n (Lloyd's Register 2014). For $t_1/t_n > 6.0$, f_{DLF} remains a constant at 1.870.

The minimum scantling (or plating thickness) stipulated by the design guideline (Lloyd's Register 2014) is given by

$$h = \sqrt{\frac{f_{DLF} P_r a b^2}{6 f_\sigma \sigma_0 (b + \frac{f_\gamma a}{1000})}}\ , \tag{6}$$

where σ_0 is the static yield stress of the material; f_σ is the material hardening factor, the value of f_σ is either 1.3 if $\sigma_0 \leq 300$ MPa or 1.2 if $\sigma_0 > 300$ MPa; and f_γ is the plate aspect ratio factor (see Fig. 6 in Lloyd's Register (2014)). It is worth emphasising that several iterations are needed to obtain a converged f_{DLF} before a final converged value for the plating thickness h can be found.

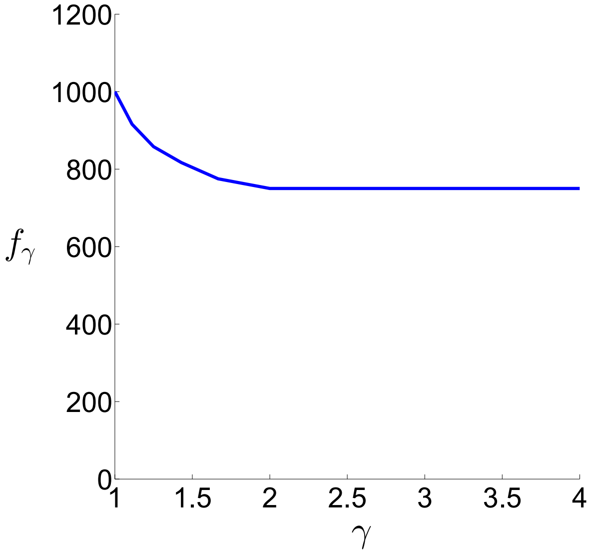

Figure 6. Value of the plate aspect ratio factor f_γ versus aspect ratio γ (Lloyd's Register 2014). For $\gamma > 2.0$, the value of f_γ remains a constant at 750.

2.2. Rationalisation of the scantling equation

The dynamic load factor f_{DLF} is defined as a ratio of maximum displacements by a structure under dynamic ($\omega_{c_{dynamic}}$) to its corresponding quasi-static conditions ($\omega_{c_{static}}$) given by (Smith and Hetherington 1994)

$$f_{DLF} = \frac{\omega_{c_{dynamic}}}{\omega_{c_{static}}}. \tag{7}$$

It is worth noting that f_{DLF} was used previously by Smith and Hetherington (1994) for a linear elastic system and the spring constant k is assumed to remain a constant throughout (Fig. 7). Multiplying the spring constant to both the numerator and denominator of Eq. 7, one obtains a ratio of the maximum resistance ($R_{dynamic}$) to its static resistance (R_{static}) as follows:

$$f_{DLF} = \frac{k\omega_{c_{dynamic}}}{k\omega_{c_{static}}} = \frac{R_{dynamic}}{R_{static}}. \tag{8}$$

Rearranging Eq. 6, to make f_{DLF} the subject, gives

$$f_{DLF} = \frac{6 f_\sigma \sigma_0 h^2 (1 + \frac{f_\gamma}{1000}\gamma)}{P_r ab}. \tag{9}$$

By a straight forward comparison of Eqs. 8 and 9, it is obvious that f_{DLF} is analogous to a factor of safety. Consider only the numerator of Eq. 9, substituting m_0 for $\sigma_0 h^2/4$ (fully plastic bending moment) and eliminating the material hardening effect (by taking $f_\sigma = 1.0$) gives

$$R_{LRN} = m_0 \cdot 24(1 + \frac{f_\gamma}{1000}\gamma) \tag{10}$$

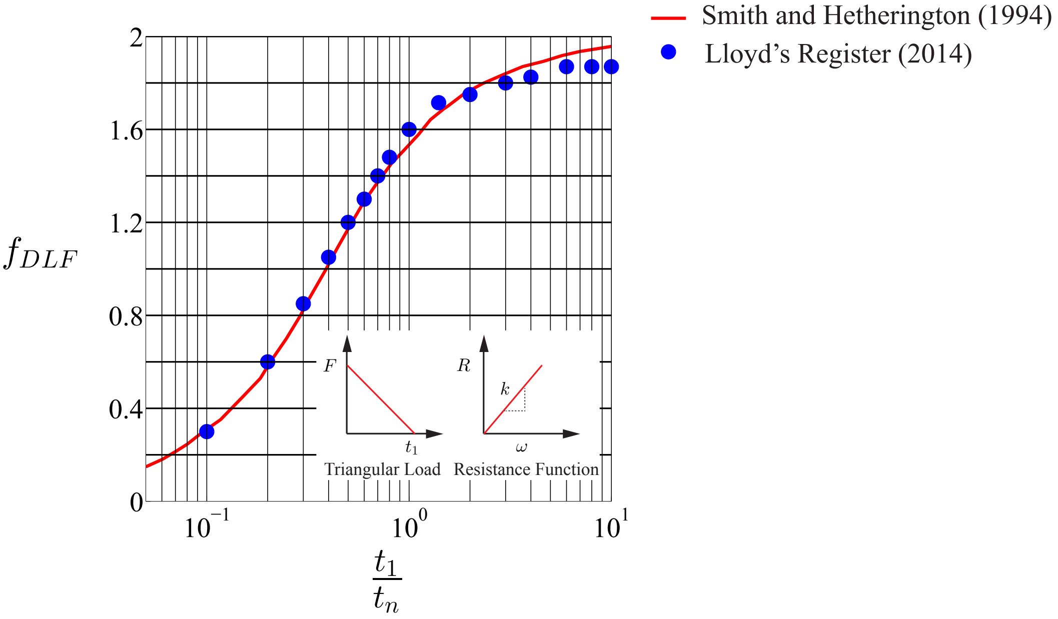

Figure 7. The dynamic load factor f_{DLF} for a linear elastic system (Smith and Hetherington 1994) compared to Lloyd's Register (2014).

– the maximum allowable resistance of a fully clamped plate with aspect ratio γ. It is also worth emphasising that for a given plating (with known material yield stress and plating thickness), the resistance R_{LRN} is a function of the aspect ratio since f_γ is also a function of γ.

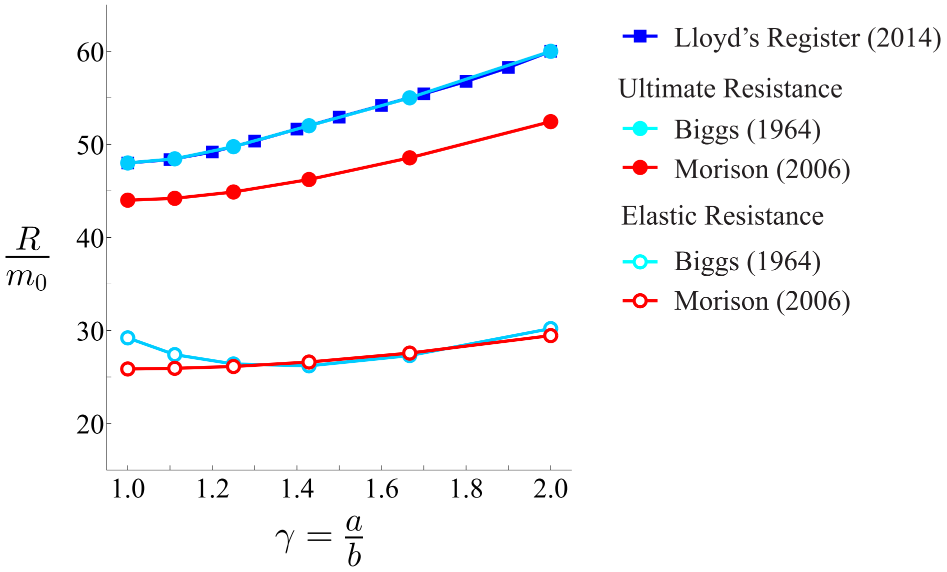

Figure 8. Comparison of resistances between design equation by the LRN and those obtained from single degree of freedom models.

Figure 8 compares the resistances predicted by Eq. 10 to those in existing literature. The blue curve -■- (Eq. 10) shows an approximate 25% rise in resistance as aspect ratio γ increases by a factor of 2. Compared to the elastic resistances (R_e) obtained from single degree of freedom models by Biggs (1964) and Morison (2006), it is clear that Eq. 10 by LRN assumes a much higher resistance than its elastic counterpart R_e. On the other hand, Eq. 10 appears to match perfectly the ultimate resistance R_u in Biggs (1964) model. In general, the resistances given in Eq. 10 are approximately 10% to 15% higher than the ultimate resistance of Morison (2006).

There are two additional resistance measures in literature that can be used for comparison. The first is from an SDOF model proposed by the US Army Corps of Engineers (1957b) which uses

$$R_{u415} = m_0 \cdot 48\left(\frac{\gamma^2 + \gamma - 1}{3\gamma - 2}\right) \tag{11}$$

to calculate the ultimate resistance of a fully clamped plate. The second is from Jones (2011) as follows:

$$R_{collapse} = m_0 \cdot 48\left(\frac{\gamma^3}{(\sqrt{3\gamma^2 + 1} - 1)^2}\right) \tag{12}$$

which gives the static collapse load of a plate, and this has the same physical meaning as an ultimate resistance. Figure 9 compares the three resistance equations. Notice that

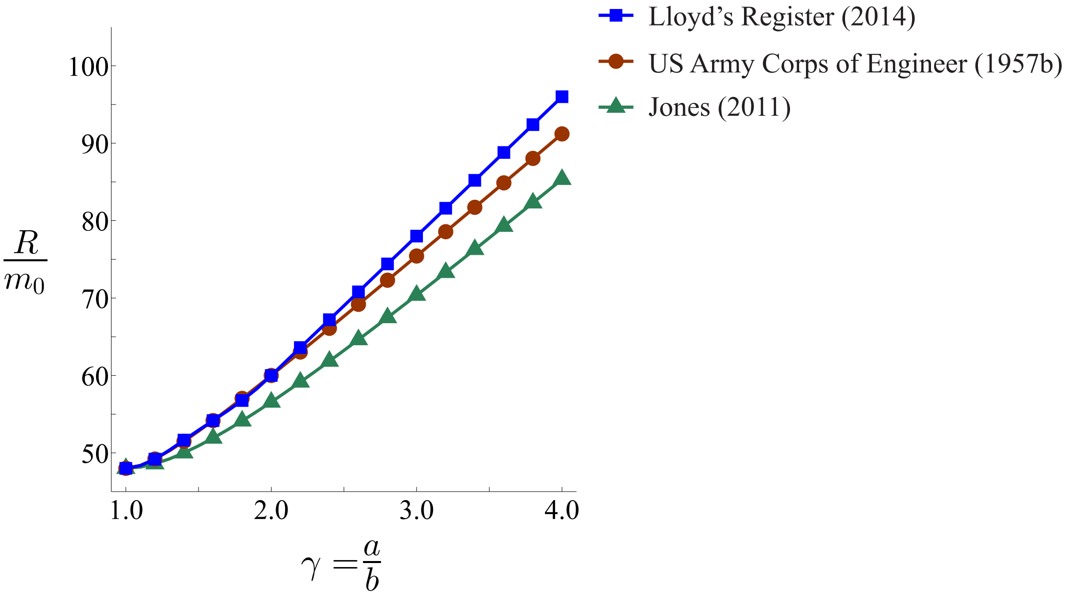

Figure 9. Comparison between the assumed resistance in the design equation by LRN to the ultimate resistance and static collapse load of fully clamped plates from literature.

all three curves start at an identical value of $48m_0$ for a plate aspect ratio of $\gamma = 1.0$. The resistance given by Eq. 12 is, in general, lower than those of Eqs. 10 and 11. As γ increases beyond $\gamma = 2.0$, the resistances between Eqs. 10 and 11 diverge - a consequence of the assumption that the plate aspect ratio factor f_γ (in Eq. 10) remains a constant value beyond $\gamma \geq 2.0$. Notwithstanding, the maximum difference between the three resistances are less that 12.5% for the entire range of γ – this is not a huge difference in engineering application.

Hence, it is reasonable to conclude that Eq. 10 represents an ultimate resistance of a plate, and Eq. 6 is based on an elastic limit state when designing against an external blast.

3. Single degree of freedom (SDOF) model

3.1. Basic principle

The basic principle is to transform the plating into an equivalent single degree of freedom system – with an equivalent mass M_E, a spring constant k_E, and an identical central deflection ω_c to the original plate structure subjected to an equivalent load $F_E(t)$ – as shown schematically in Fig. 10 (US Army Corps of Engineers 1957a,b). The ratio of the equivalent mass M_E to the actual mass of the plate M is the *mass factor* given by $K_m \triangleq M_E/M$; whilst, the ratio of the equivalent load $F_E(t)$ to the actual load on the plate $F(t)$ is the *load factor* given by $K_l \triangleq F_E(t)/F(t)$. Note that the stiffness of the plate k is numerically equal to the load (same distribution as $F(t)$) needed to give a unit central deflection. A relationship exists between the equivalent spring constant k_E and plate stiffness k given by $K_l \triangleq k_E/k$. The load (K_l) and mass (K_m) factors are derived for each phase of the deformation, by using their corresponding shape functions $\phi(x,y)$, through

$$K_l^{()} = \frac{\int_{-\frac{b}{2}}^{\frac{b}{2}} \int_{-\frac{a}{2}}^{\frac{a}{2}} \phi(x,y) dxdy}{ab}, \tag{13}$$

and

$$K_m^{()} = \frac{\int_{-\frac{b}{2}}^{\frac{b}{2}} \int_{-\frac{a}{2}}^{\frac{a}{2}} \phi(x,y)^2 dxdy}{ab}, \tag{14}$$

where the superscript () = I, II, III or IV indicates the phase of deformation, $\phi(x,y)$ is shape function of each phase. Since the equivalent system has the same central deflection ω_c as the original plate system, the equation of motion of the equivalent system is given by

$$M_E \ddot{\omega}_c + k_E \omega_c = F_E(t), \tag{15}$$

which can be rewritten as

$$\frac{K_m^{()}}{K_l^{()}} M \ddot{\omega}_c + k\omega_c = F(t). \tag{16}$$

To the best of the authors' knowledge, all SDOF models of fully-clamped plate in existing literature consider only 3 phases of deformation (elastic, elasto-plastic and plastic bending phases), with a corresponding resistance curve (····) as shown in Fig. 11. Typically, a constant maximum resistance is used to characterise the plastic bending

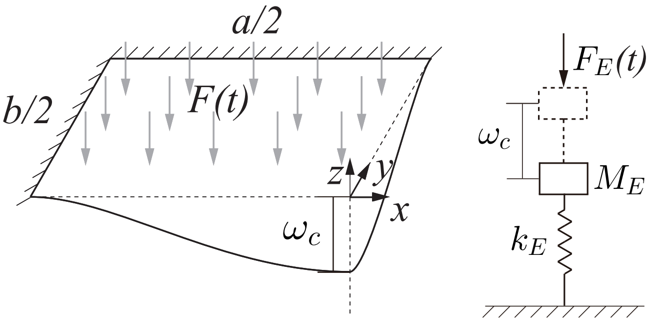

(a) (b)

Figure 10. Transformation of a fully fixed plate into a mass-spring system (US Army Corps of Engineers 1957a,b): (a) a quarter of the plate that shows the magnitude of central deflection ω_c under uniformly distributed loading $F(t)$; (b) the equivalent system has an equivalent mass M_E and a spring constant k_E, and the same central deflection ω_c to (a) is obtained when subjected to an equivalent load $F_E(t)$.

phase during which plastic bending occurs along the yield (or hinge) lines. However, Yu and Chen (1992) highlighted that in-plane membrane forces are highly significant during large plastic deformation since they contribute towards dissipating a significant amount of energy and, thus, stiffens the structure. Inspired by this, a fourth plastic membrane phase will be introduced into the SDOF model, to be developed here, which uses the in-panel membrane forces to counter the lateral transverse loads when the central deflection of the plate exceeds a critical value. For simplicity, we ignore the coupling between bending and membrane forces on the hinge lines - the same is also adopted by Det Norske Veritas (2010) for beams. The resistance curve of the new 4-phases SDOF model is shown as a solid line (—) in Fig. 11. For simplicity, a piece-wise linear approximation of the resistance is assumed for each phase.

For each phase of deformation, Eq. 16 has to be modified as follows:

- Elastic

$$\frac{K_m^{\mathrm{I}}}{K_l^{\mathrm{I}}} M\ddot{\omega}_c + k^{\mathrm{I}}\omega_c = F(t), \tag{17}$$

- Elasto-plastic

$$\frac{K_m^{\mathrm{II}}}{K_l^{\mathrm{II}}} M\ddot{\omega}_c + k^{\mathrm{II}}(\omega_c - \omega_{ce}) + R_e = F(t), \tag{18}$$

- Plastic bending

$$\frac{K_m^{\mathrm{III}}}{K_l^{\mathrm{III}}} M\ddot{\omega}_c + R_u = F(t), \tag{19}$$

- Plastic membrane

$$\frac{K_m^{\mathrm{IV}}}{K_l^{\mathrm{IV}}} M\ddot{\omega}_c + k^{\mathrm{IV}}(\omega_c - \omega_{cm}) + R_u = F(t), \tag{20}$$

where, ω_c is the central deflection; M is the plating mass; K_m^{I}, K_m^{II}, K_m^{III} *and* K_m^{IV} are the mass factors; K_l^{I}, K_l^{II}, K_l^{III} *and* K_l^{IV} are the load factors; k^{I}, k^{II} *and* k^{IV} are the spring constants; R_e and R_u are the elastic and ultimate resistances of the plating; ω_{ce} is the maximum elastic deflection, $\omega_{ce} = R_e/k^{\mathrm{I}}$; ω_{cu} is the maximum elasto-plastic deflection given by $\omega_{cu} = (R_u - R_e)/k^{\mathrm{II}} + R_e/k^{\mathrm{I}}$; ω_{cm} is the maximum plastic bending deflection which is equal to the plating thickness h; $F(t)$ is the dynamic load given by

$$F(t) = P_r(t)ab, \tag{21}$$

and $P_r(t)$ is the reflected overpressure curve as described in Section 2.1

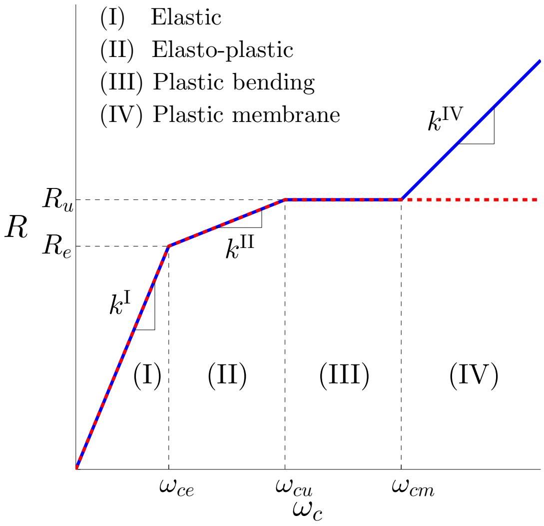

Figure 11. Resistance curves for ···· traditional SDOF models (with 3 phases of deformations) with a constant maximum resistance Ru, and — for the current SDOF model with 4 phases of deformation, including a new membrane phase.

3.2. 4 phases of deformations

3.2.1. Phase I: Elastic deformation

Following Timoshenko and Woinowsky-Krieger (1959), the elastic deformation of a fully clamped rectangular plate is treated as a superposition of deformations by three simply supported plates of identical dimensions. The first is a simply supported plate with the same imposed loading as the original plate, and other two with bending moments applied to their two opposite edges to simulate the fixed boundaries shown schematically in Fig. 12.

The deflection of a fully clamped plate under uniform distributed pressure q can be

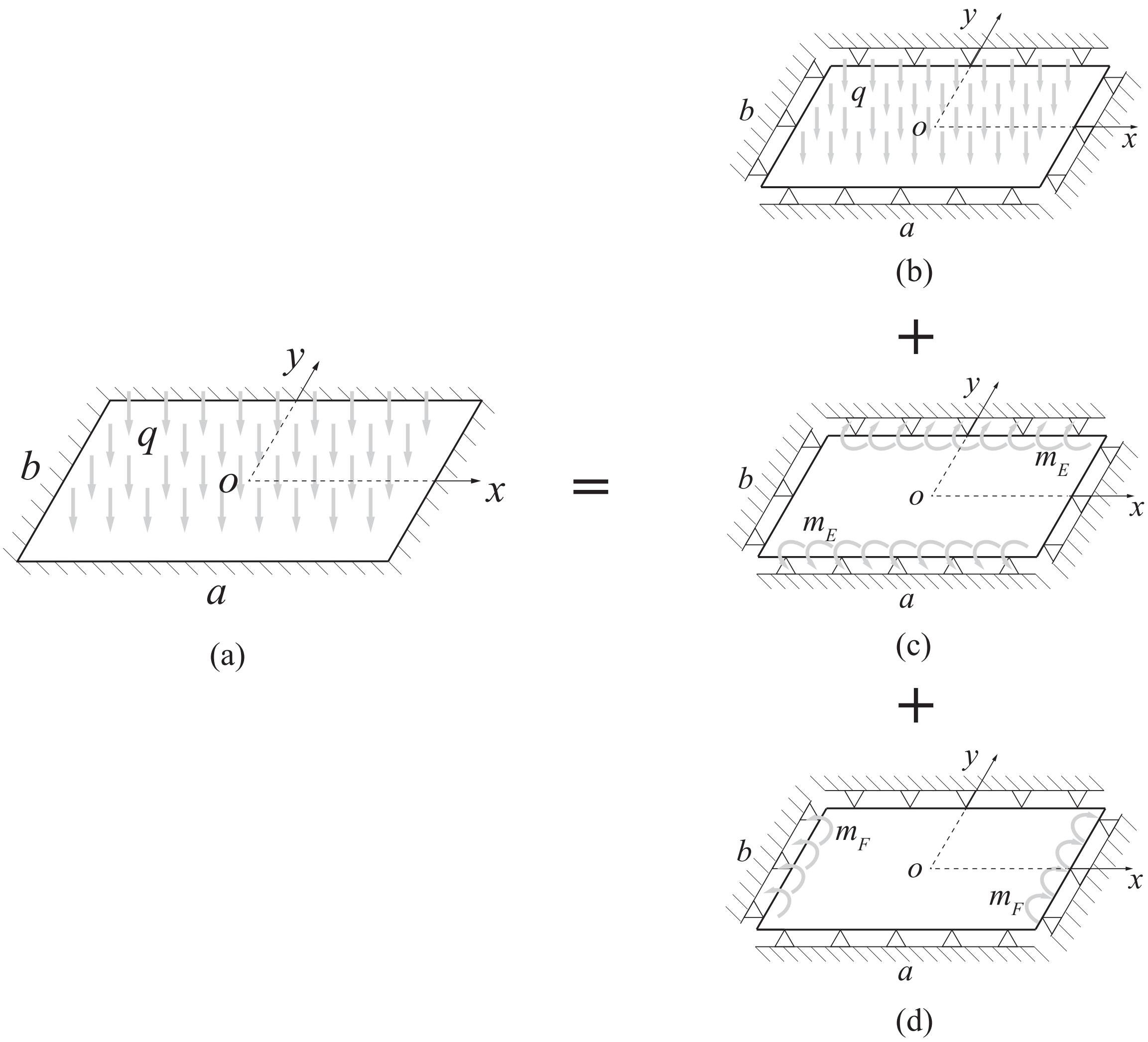

Figure 12. Separation of deformation for a fully clamped plate subjected to a uniformly distributed pressure loading: (a) fully clamped plate under distributed pressure q; (b) simply supported plate subjected to a distributed pressure q; (c) simply supported plate with a uniform bending m_E along its longer edges; (d) simply supported plate with a uniform bending m_F along its shorter edges.

written as a superposition of 3 parts (Timoshenko and Woinowsky-Krieger 1959):

$$\omega_e = \omega_{e0} - \omega_{e1} - \omega_{e2}, \tag{22}$$

where ω_{e0} is the deflection of a simply supported plate subjected to a uniformly distributed pressure q (Fig. 12b); and, ω_{e1} and ω_{e2} is the corresponding deflection of the simply supported plate with bending moment applied on its two opposite edges as shown in Figs. 12c and 12d, respectively. The deflection functions are as follows (Timoshenko and Woinowsky-Krieger 1959):

$$\omega_{e0} =\frac{4qa^4}{\pi^5 D}\sum_{i=1,3,5,\ldots}^{\infty}\frac{(-1)^{(i-1)/2}}{i^5}\cos\frac{i\pi x}{a}\cdot \left(1-\frac{\alpha_i\tanh\alpha_i+2}{2\cosh\alpha_i}\cosh\frac{i\pi y}{a}+\frac{1}{2\cosh\alpha_i}\frac{i\pi y}{a}\sinh\frac{i\pi y}{a}\right), \tag{23}$$

$$\omega_{e1} =\frac{a^2}{2\pi^2 D}\sum_{i=1,3,5,\ldots}^{\infty}E_i\frac{(-1)^{(i-1)/2}}{i^2\cosh\alpha_i}\cos\frac{i\pi x}{a}\cdot \left(\frac{i\pi y}{a}\sinh\frac{i\pi y}{a}-\alpha_i\tanh\alpha_i\cosh\frac{i\pi y}{a}\right), \tag{24}$$

and

$$\omega_{e2} =\frac{b^2}{2\pi^2 D}\sum_{i=1,3,5,\ldots}^{\infty}F_i\frac{(-1)^{(i-1)/2}}{i^2\cosh\beta_i}\cos\frac{i\pi y}{b}\cdot \left(\frac{i\pi x}{b}\sinh\frac{i\pi x}{b}-\beta_i\tanh\beta_i\cosh\frac{i\pi x}{b}\right), \tag{25}$$

where $D \triangleq Eh^3/12(1-\nu^2)$ is flexural rigidity of the plate per unit length; i is a summation index (a maximum of 101 is used in this study); $\alpha_i = i\pi b/2a$ and $\beta_i = i\pi a/2b$; E_i and F_i are internal parameters that must be calculated numerically by equating the combined edge rotations of the plate to zero.

The elastic phase ends when any material point on the plate reaches yield (US Army Corps of Engineers 1957a,b). However, it is difficult to perform a full-field stress analysis of the plate at every time increment. To simplify the analysis, we follow Morison's (Morison 2006) termination principle that the bending moment m_E and m_F in Figs. 12c and 12d is equal to the unit plastic bending moment $m_0 = \sigma_0 h^2/4$, at the elastic limit. According to Eq. 22, the elastic limit is reached when the central deflection of the fully clamped plate is equal to that of a simply supported plate subjected to the same pressure with unit plastic bending moment on four edges as follows:

$$\omega_{cec} = \omega_{ces} - \omega_{cbs1} - \omega_{cbs2} \tag{26}$$

where ω_{cec}, ω_{ces}, ω_{cbs1} and ω_{cbs2} are the central deflections of a fully clamped, simply supported and edge-loaded plates (by uniform moment m_0 for m_E and m_F in Fig. 12 b and c) given, respectively, by

$$\begin{aligned}
\omega_{cec} &= \frac{R_e}{k^{\mathrm{I}}}, \\
\omega_{ces} &= \frac{R_e}{k^{\mathrm{II}}}, \\
\omega_{cbs1} &= \frac{abm_0}{\pi^2 D} \sum_{i=1,3,5,\ldots}^{\infty} \frac{(-1)^{(i-1)/2} \tanh \alpha_i}{i^2 \cosh \alpha_i} \quad \text{and} \\
\omega_{cbs2} &= \frac{abm_0}{\pi^2 D} \sum_{i=1,3,5,\ldots}^{\infty} \frac{(-1)^{(i-1)/2} \tanh \beta_i}{i^2 \cosh \beta_i}.
\end{aligned} \tag{27}$$

3.2.2. Phase II: Elasto-plastic deformation

Following Biggs (1964) and US Army Corps of Engineers (1957a,b), it is assumed that the deformation shape of a fully clamped plate is identical to a simply supported plate. The deformation function of a simply supported plate subjected to a uniformly distributed pressure q – see Fig. 12b – is given by (Timoshenko and Woinowsky-Krieger 1959)

$$\omega_{ep} = \frac{16q_0}{\pi^6 D} \sum_{i=1}^{\infty} \sum_{j=1}^{\infty} \frac{\sin(\frac{i\pi}{a}x + \frac{i\pi}{2}) \sin(\frac{j\pi}{b}y + \frac{j\pi}{2})}{ij(\frac{i^2}{a^2} + \frac{j^2}{b^2})^2}. \tag{28}$$

As shown in Fig. 11, the resistance of the system increases linearly with central deflection ω_c, but its slope k^{II} is smaller than its elastic counterpart k^I. The elasto-plastic phase ends when the resistance reaches the ultimate resistance R_u, which is calculated from the plastic bending phase (Biggs 1964).

3.2.3. Phase III: Plastic bending deformation

Figure 13 shows the yield line pattern proposed by Jones (2011) for a perfectly-plastic plate. This same yield line pattern is also assumed for the plastic bending phase in the current SDOF model. The plate is separated into four parts, with the yield lines located along the boundaries and in the plate interior. Under lateral pressure loading, the rigid portions of the plate rotate about the yield (hinge) lines.

Following Yu and Chen (1992), the shape function for the fully-plastic bending phase

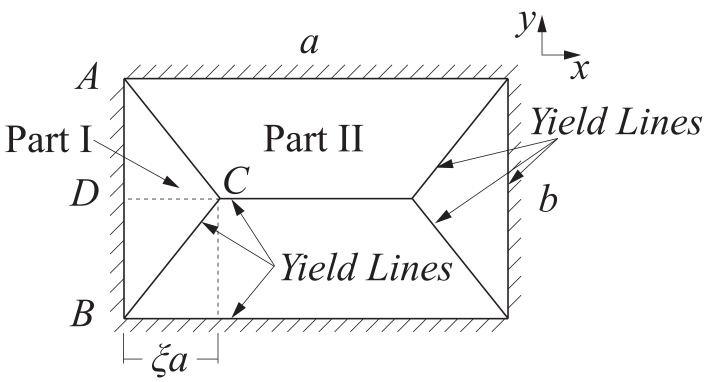

Figure 13. Yield line pattern of a rectangular plate deforming in the fully-plastic bending phase (Jones 2011).

is as follows:

$$
\phi_p = \begin{cases}
\begin{cases}
\frac{b+2y}{b} & \text{if } y \in \big[-\frac{1}{2}b, -\frac{b}{2\xi a}(\xi a - \frac{1}{2}a - x)\big) \\
\frac{a+2x}{2\xi a} & \text{if } y \in \big[-\frac{b}{2\xi a}(\xi a - \frac{1}{2}a - x), \frac{b}{2\xi a}(\xi a - \frac{1}{2}a - x)\big) \\
\frac{b-2y}{b} & \text{if } y \in \big[\frac{b}{2\xi a}(\xi a - \frac{1}{2}a - x), \frac{1}{2}b\big]
\end{cases} & \text{if } x \in \big[-\frac{1}{2}a, -\frac{1}{2}a + \xi a\big) \\
\begin{cases}
\frac{b+2y}{b} & \text{if } y \in \big[-\frac{1}{2}b, 0\big) \\
\frac{b-2y}{b} & \text{if } y \in \big[0, \frac{1}{2}b\big]
\end{cases} & \text{if } x \in \big[-\frac{1}{2}a + \xi a, \frac{1}{2}a - \xi a\big) \\
\begin{cases}
\frac{b+2y}{b} & \text{if } y \in \big[-\frac{1}{2}b, -\frac{b}{2\xi a}(\xi a - \frac{1}{2}a - x)\big) \\
\frac{a-2x}{2\xi a} & \text{if } y \in \big[-\frac{b}{2\xi a}(\xi a - \frac{1}{2}a - x), \frac{b}{2\xi a}(\xi a - \frac{1}{2}a - x)\big) \\
\frac{b-2y}{b} & \text{if } y \in \big[\frac{b}{2\xi a}(\xi a - \frac{1}{2}a - x), \frac{1}{2}b\big]
\end{cases} & \text{if } x \in \big[\frac{1}{2}a - \xi a, \frac{1}{2}a\big]
\end{cases} \tag{29}
$$

where $\xi \triangleq (\sqrt{1 + 3a^2/b^2} - 1)/(2a^2/b^2)$ is a dimensionless parameter defining the size of rigid zones. The unit plastic moment $m_0 = \sigma_0 h^2/4$ is assumed to act along the yield lines.

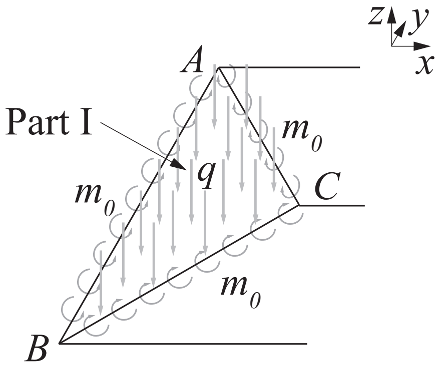

Figure 14. The loading distribution on Part I during the plastic bending phase, on which pressure load q and bending m_0 on yield lines achieve moment equilibrium against edge AB.

Under static loading condition, bending moments created by the pressure load is in balance with the resisting moments from the yield lines. Taking Part I for instance (see Fig. 14), the pressure load q and bending m_0 on yield lines achieve moment equilibrium against edge AB given by

$$\frac{1}{3}\xi a \cdot \frac{1}{2}\xi ab \cdot q = 2m_0 b. \tag{30}$$

Therefore, the allowable pressure under this condition is $q = \frac{12}{\xi^2 a^2} m_0$, and the maximum resistance R_u of the plate is given by (US Army Corps of Engineers 1957a)

$$R_u = qab = \frac{12b}{\xi^2 a} m_0. \tag{31}$$

3.2.4. Phase IV: Plastic membrane deformation

In the plastic membrane phase, the plate deforms with the same yield line pattern as previously (Fig. 13 and Eq. 29). When the deflection of a plate approaches or exceeds its thickness, the edge supports restrain the movement in its mid-plane and membrane forces are induced which dissipate energy and stiffen the structure (Yu and Chen 1992).

In the current model, the membrane force (resistance) is assumed to increase linearly with central deflection, and the magnitude of the total membrane force is calculated using energy conservation. Taking the upper half of Part I (ADC), for example, the work done by the distributed pressure q_0 is given by

$$W_q = q_0(\omega_c - \omega_{cm}) \int_0^{\frac{1}{2}b} \int_0^{\xi a} \frac{x}{\xi a} dx dy = q_0(\omega_c - \omega_{cm}) \frac{\xi ab}{4}, \tag{32}$$

where ω_{cm} is the critical central deflection when the membrane forces come into effect (Yu and Chen 1992). The energy dissipated by the bending moment about the hinge lines is

$$W_b = \frac{1}{2} 2bm_0 \frac{\omega_c - \omega_{cm}}{\xi a}. \tag{33}$$

As seen in Fig. 15, the extension at point y is $\frac{b-2y}{\xi ab}(\omega_c^2 - \omega_{cm}^2)$; hence, the energy absorbed by the membrane force is

$$W_m = n_0 \int_0^{\frac{1}{2}b} \frac{b-2y}{\xi ab}(\omega_c^2 - \omega_{cm}^2) dy = \frac{bn_0}{4\xi a}(\omega_c^2 - \omega_{cm}^2) \tag{34}$$

where $n_0 \overset{\Delta}{=} \sigma_0 h$ is the unit membrane force. By energy conservation

$$W_q = W_b + W_m, \tag{35}$$

the distributed pressure is $q = \frac{1}{\xi^2 a^2}[4m_0 + n_0(\omega_c + \omega_{cm})]$, and the resistance in this phase is

$$R = qab = \frac{b}{\xi^2 a}[4m_0 + n_0(\omega_c + \omega_{cm})]. \tag{36}$$

Here, ω_{cm} is the central deflection corresponding to the start of the plastic membrane phase. To determine the value for ω_{cm}, one equates Eqs. 31 to 36, and obtain $\omega_{cm} = h$.

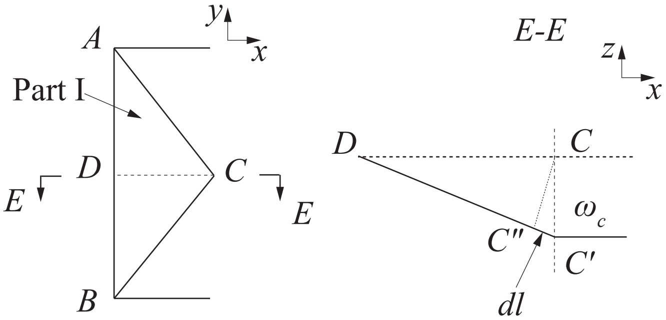

Figure 15. The extension of plastic hinges in the plastic membrane phase, and on the cross-section CD the extension dl is regarded as a function of central deflection ω_c (adapted from Jones (2011)).

3.3. Transformation factors for the 4-phases SDOF model

Through $\phi(x, y) = \omega(x, y)/\omega_c$, the deformation function in the elastic (Eq. 22) and elasto-plastic (Eq. 28) phases are transformed into corresponding shape function. Substituting Eqs. 22, 28 and 29 into Eqs. 13 and 14 give the corresponding load and mass transformation factors. Additionally, the spring constant k is equal to the load (qab) needed to cause a unit central deflection ($\omega_c = 1.0$) from the deformation functions in Eqs 22 and 28.

Table 1 tabulates the transformation factors derived for the new 4-phases SDOF model developed here. Data for plate aspect ratio γ of up to 4.0 (in increments of 0.5), they are often encountered in ship platings, are provided. Another important feature of the table is that the elastic and elasto-plastic spring constants (k_{el} and k_{ep}) are now non-dimensionalised with the flexural rigidity $D = Eh^3/(12(1 - \nu^2))$, which makes it more convenient for comparing plates of different materials.

The present load and mass factors in the elastic (K_l^{I} and K_m^{I}) and elasto-plastic (K_l^{II} and K_m^{II}) phases are nearly identical to those by Morison (2006) where the finite element method was used in their derivations. However, both factors differ significantly from those tabulated by Biggs (1964). On the other hand, all three SDOF models (present, Morison and Biggs) have nearly identical spring constants k^{I} and k^{II}, and elastic resistances R_e. However, the new transformation factors for the plastic bending phase (K_l^{III}, K_m^{III} and R_u) are different to previous models and this is due to differences in the assumed yield line patterns.

3.4. Validation of the 4 phases SDOF model

3.4.1. Elastic deformation in the dynamic régime

Houlston et al. (1985) performed blast tests on rectangular steel plates that deformed

Table 1. Transformation factors for a monolithic metal plate with fully clamped boundary.

	Elastic				Elasto-plastic				Plastic-bending		Plastic-membrane		
γ	K_l^{I}	K_m^{I}	$k^{\mathrm{I}}/(D/b^2)$	R_e/m_0	K_l^{II}	K_m^{II}	$k^{\mathrm{II}}/(D/b^2)$	R_u/m_0	K_l^{III}	K_m^{III}	K_l^{IV}	K_m^{IV}	k^{IV}/n_0
1.0	0.3075	0.1824	790.3139	26.3392	0.4191	0.2623	246.1628	48.0000	0.3333	0.1667	0.3333	0.1667	4.0000
1.0[1]	0.3080	0.1820	790.3088	25.8600	0.4190	0.2620	246.1345	44.0000	0.3180	0.1600	-	-	-
1.0[2]	0.3300	0.2100	791.7750	29.2000	0.4600	0.3100	246.3300	48.0000	0.3300	0.1700	-	-	-
1.5	0.3200	0.1927	682.8984	27.3463	0.4239	0.2668	194.1994	50.9076	0.3679	0.2012	0.3679	0.2012	4.2423
2.0	0.3460	0.2157	789.5900	29.9832	0.4348	0.2772	197.4591	56.5629	0.3914	0.2248	0.3914	0.2248	4.7136
2.0[1]	0.3470	0.2160	789.1358	29.4500	0.4350	0.2780	197.4550	52.4400	0.3790	0.2170	-	-	-
2.0[2]	0.4300	0.3100	787.8650	30.2000	0.5500	0.4100	196.4775	42.0000	0.4200	0.2500	-	-	-
2.5	0.3750	0.2435	957.2529	33.7449	0.4491	0.2911	217.4708	63.2282	0.4082	0.2415	0.4082	0.2415	5.2690
3.0	0.4003	0.2691	1146.2500	38.2760	0.4647	0.3069	245.2421	70.3697	0.4205	0.2537	0.4205	0.2537	5.8641
3.5	0.4199	0.2895	1340.4980	43.3433	0.4804	0.3232	277.3498	77.7725	0.4300	0.2633	0.4300	0.2633	6.4810
4.0	0.4346	0.3049	1534.5720	48.7729	0.4951	0.3390	312.0454	85.3333	0.4375	0.2708	0.4375	0.2708	7.1111

$D = Eh^3/(12(1-\nu^2))$, $m_0 = \sigma_0 h^2/4$ and $n_0 = \sigma_0 h$

1: Morison (2006); 2: Biggs (1964)

elastically. The key geometric parameters of the plate and its material properties are summarised in Table 2. In their blast test, pressures were recorded at different points on the plate surface which revealed that the loading was approximately uniformly-distributed. Figure 16 shows the loading pressure curve on the plate surface. The positive phase of the blast wave lasted around 2.2 ms and this was followed by a long negative suction phase. The loading pressure peaked at 57.5 KPa in the beginning, and decayed until the second peak at approximately 0.9 KPa. The second peak pressure was a result of the blast wave reflection from the test environment.

Table 2. Key parameters of the blast test conducted by Houlston et al. (1985)

Plate length (a)	0.508 m
Plate width (b)	0.508 m
Plate thickness (h)	0.0034 m
Plate aspect ratio (γ)	1.0
Density (ρ)	2710.6 kg/m^3
Young's modulus (E)	207 GPa
Poisson's ratio (ν)	0.3
Static yield stress (σ_0)	345 MPa

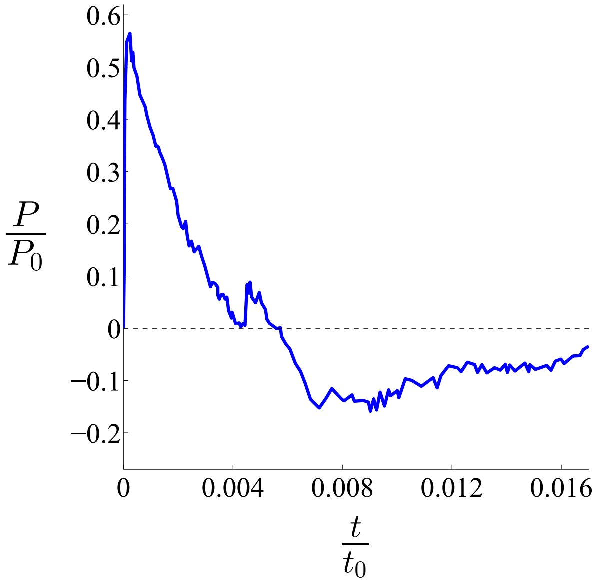

Figure 16. The reflected pressure-time history recorded by Houlston et al. (1985). Note that P_0 is the atmospheric pressure 101.3 KPa and t_0 is taken as 0.4 s

Since the experimental results showed that the plate only deforms elastically, the equation of motion in Eq. 16 becomes

$$\frac{K_m^{\mathrm{I}}}{K_l^{\mathrm{I}}} M\ddot{\omega}_c + k^{\mathrm{I}}\omega_c = P(t)ab. \tag{37}$$

From Table 1, the relevant transformation factors are obtained as follows: $K_l^{\mathrm{I}} = 0.1824$, $K_m^{\mathrm{I}} = 0.3075$ and $k^{\mathrm{I}} = 790.3139 \times D/b^2 = 671085.3$ KN/m. The mass of the plate (M) is 2.378 kg, and the pressure values $P(t)$ are read from Fig. 16 at time increment of

$\Delta t = 0.01$ ms. Equation 37 is then solved numerically using the fourth-order Runge-Kutta method (Dechaumphai and Wansophark 2011).

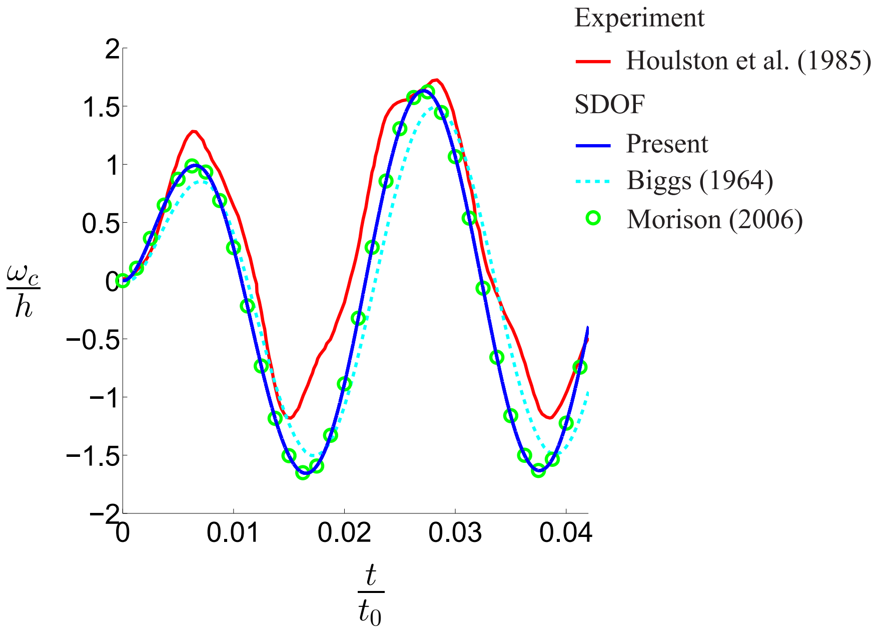

Figure 17. Comparison of the SDOF predictions against experimental data by Houlston et al. (1985) test. Note that the plate thickness h is 0.0034 m and t_0 is taken to be 0.4 s.

Figure 17 compares the SDOF predictions against recorded central deflections in the test. The prediction by the current SDOF follows a similar trend to the experiment; and, the predicted peak deflection is $5.5mm$ compared to $5.8mm$ in experiment. The differences between the two curves can be attributed to inaccuracies in the recorded pressure and limitations of the SDOF approach in accurately predicting harmonic-type motions. It is also worth noting both the current and Morison's (Morison 2006), which have nearly identical transformation factors, provide a more accurate prediction of the peak deflection compared to Biggs (1964).

3.4.2. Plastic deformation in the impulsive régime

In an air blast, the permanent central deflection of a steel plate is typically several times its thickness. A series of laboratory-scale experiments were conducted by Olson et al. (1993) and Nurick and Shave (1996) on rectangular plates of $89 \times 89 \times 1.6$ mm subjected to an impulsive load. Key geometric parameters and material properties of the plates are summarised in Table 3.

To apply the current SDOF model, the resistance of the plate must first be evaluated. The parameters needed to construct the resistance curve, as shown in Fig. 11, are provided in Table 4. Deformation of the plate ceases when the initial kinetic energy ($\frac{1}{2}MV_0^2$) it acquired fromthe blast is expended through resistance offered by the plate (the area under the resistance curve) such that (Det Norske Veritas 2010)

$$\frac{1}{2}MV_0^2 = \int_0^{\omega_{cmax}} R(\omega_c)d\omega_c. \tag{38}$$

Table 3. Key parameters of the blast tests by Olson et al. (1993) and Nurick and Shave (1996)

Plate length (a)	0.089 m
Plate width (b)	0.089 m
Plate thickness (h)	0.0016 m
Plate aspect ratio (γ)	1.0
Density (ρ)	2830 kg/m^3
Young's modulus (E)	197 GPa
Poisson's ratio (ν)	0.3
Static yield stress (σ_0)	237 MPa
Rupture strain (ε_{rup})	0.31

Table 4. Key parameters of the resistance curve

Elastic spring constant k^{I}	12740 KN/m
Elasto-plastic spring constant k^{II}	3968 KN/m
Plastic membrane spring constant k^{IV}	2097 KN/m
Maximum elastic resistance R_e	6627 N
Ultimate resistance R_u	12077 N
Maximum elastic deflection ω_{ce}	0.0005 m
Maximum elasto-plastic deflection ω_{cu}	0.0014 m
Maximum plastic bending deflection ω_{cm}	0.0016 m

Figure 18 compares the predicted central deflection by the different SDOF models (current, Morison and Biggs) for different non-dimensional impulse I^*. It is evident that predictions by the traditional 3-phases SDOF model by Biggs (1964) and Morison (2006) significantly overestimate the plate deflection. The present 4-phases SDOF model gives a much closer match to the experimental data but they, too, shows discrepancies. The discrepancy arises from the fact that only the permanent deflections are recorded in the experiments whilst the SDOF model includes both elastic and elasto-plastic deformations. Therefore, a corrected deflection curve ····, one that only considers the plastic phases (III and IV), as suggested in US Navy (1990), gives a much closer prediction of the experimental data. Moreover, the effects of material strain rate - there is no straightforward means to account for this in a SDOF approximation - were also neglected which further contributes to the aforementioned discrepancy.

Next, the transition between mode I (plastic) and mode II (tearing) failures is also compared. Experimental results have revealed that the tearing (mode II failure) of a rectangular plate initiates along the midspan of its longer edge. There are various theories that had been proposed to explain the tearing mechanism, with the simple maximum tensile strain criterion being the simplest and most commonly used. When the tensile strain along the midspan of its longer edge is greater than the rupture strain of the material, tearing occurs. Wen (1998) proposed a method to link the maximum tensile strain to the predicted central deflection and, for a fully clamped rectangular plate, this is given by

$$\varepsilon_{max} = \frac{2\pi\omega_c^2}{ab}. \tag{39}$$

Once ε_{max} reaches the rupture strain ε_{rup}, the plate tears and, consequently, loses its water- or gas-tight capabilities. From Fig. 18, the threshold velocity needed to cause

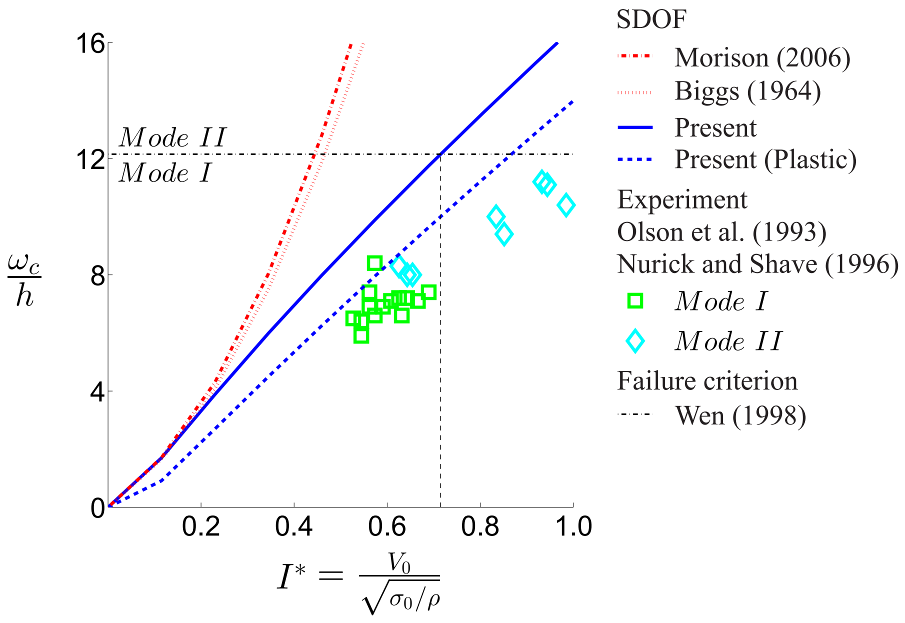

Figure 18. Comparison of different SDOF model predictions with experimental data from literature. Transition between mode I and mode II failures is determined by the value of central deflection.

Mode II failure was found to be 126.9 m/s – this is 16.6% higher than the experimental value of 108.8 m/s. Therefore; for a given rectangular plate with a rupture strain ε_{rup}, the maximum allowable central deflection ω_{cmax} needed to avoid the mode II failure could be determined from Eq. 39 as follows:

$$\frac{\omega_{cmax}}{h} = \sqrt{\frac{ab\varepsilon_{rup}}{2\pi h^2}}. \tag{40}$$

4. Finite element (FE) model

4.1. Ductile damage

In this section, the FE method is used to model the large inelastic deformation and failure of ship platings. The FE model incorporates *Progressive Damage and Failure* (Abaqus/Explicit 2010) which enables ductile damage of an element to be captured; making it possible to model tensile tearing (or mode II failure) of the ship plating from its support. The initiation of ductile damage is controlled by a state variable Ω given by

$$\Omega = \int \frac{d\bar{\varepsilon}^{pl}}{\bar{\varepsilon}_d^{pl}(\eta, \dot{\bar{\varepsilon}}^{pl})}, \tag{41}$$

where the damage initiation strain $\bar{\varepsilon}_d^{pl} = \bar{\varepsilon}_d^{pl}(\eta, \dot{\bar{\varepsilon}}^{pl})$ is the equivalent plastic strain at the onset of ductile damage. If strain rate effects $\dot{\bar{\varepsilon}}^{pl}$ can be neglected, then the damage initiation strain $\bar{\varepsilon}_d^{pl}(\eta)$ is given by (Pavlovic et al. 2013)

$$\bar{\varepsilon}_d^{pl}(\eta) = \bar{\varepsilon}_d^{pl} e^{-\beta(\eta - \frac{1}{3})}, \tag{42}$$

where $\eta \in [-\frac{1}{3}, \frac{1}{3}]$ is the stress triaxiality of the element; β is a material parameter equal to 1.5 for steels; and, $\bar{\varepsilon}_d^{pl}$ is value of the damage initiation strain under uniaxial tension ($\eta = \frac{1}{3}$).

After the initiation of damage, the material stiffness of an element is decreased according to the scalar damage equation given by

$$\sigma = (1 - \Pi)\bar{\sigma}, \tag{43}$$

where Π is the damage variable and $\bar{\sigma}$ is the effective stress tensor. The damage variable Π is given by

$$\dot{\Pi} = \frac{l_e \dot{\bar{\varepsilon}}^{pl}}{\bar{u}_f^{pl}}, \tag{44}$$

where l_e is the characteristic length of the element; $\dot{\bar{\varepsilon}}^{pl}$ is the strain rate; $\bar{u}_f^{pl}$ is the displacement at failure, and

$$\bar{u}_f^{pl} = l_e \bar{\varepsilon}_f^{pl}, \tag{45}$$

where $\bar{\varepsilon}_f^{pl}$ is the failure strain of the element. When the effective plastic strain reaches the value $\bar{\varepsilon}_f^{pl}$, the element stiffness is fully degraded and is removed from the mesh. The damage parameters – initial strain $\bar{\varepsilon}_d^{pl}$ and failure strain $\bar{\varepsilon}_f^{pl}$ – are critical to accurately model plate failure.

It is also worth emphasizing that when using shell elements, such as S4R (Abaqus/Explicit 2010) in the present study, the values for $\bar{\varepsilon}_d^{pl}$ and $\bar{\varepsilon}_f^{pl}$ are mesh dependent. Marinatos and Samuelides (2015) had previously shown that the critical strains are functions of the element size ratio l_e/h given by

$$\bar{\varepsilon}_d^{pl}, \bar{\varepsilon}_f^{pl} = \delta_1(log\frac{l_e}{h})^3 + \delta_2(log\frac{l_e}{h})^2 + \delta_3(log\frac{l_e}{h}) + \delta_4, \tag{46}$$

where l_e is the characteristic length of the element; h is the thickness of the shell element; δ_1, δ_2, δ_3 and δ_4 are the material parameters. The failure criteria that are based on the critical strains are often known as the *Germanischer Lloyd Criterion* (Ehlers et al. 2008) in the marine community.

Additionally, the mechanical properties of metals, such as mild steel, are dependent on the rate of loading, also known as viscoplasticity (Dunne and Petrinic 2005). This causes the dynamic yield stress of steel to increase significantly with the rate of straining. The current FE model uses the empirical Cowper-Symonds power law equation given by (Jones 2011)

$$\sigma_d = \sigma_0(1 + \frac{\dot{\varepsilon}}{\dot{\varepsilon}_0})^{1/r}, \tag{47}$$

where $\dot{\varepsilon}_0$ and r are the material constants. For mild steel, $\dot{\varepsilon}_0 = 40.4\ s^{-1}$ and $r = 5$.

4.2. Calibration of damage parameters

The damage parameters $\bar{\varepsilon}_d^{pl}$ and $\bar{\varepsilon}_f^{pl}$ for mild steel is obtained through the FE modelling of a uniaxial tensile test coupon (Yu and Jones 1991). Figure 19 shows a typical tensile test coupon - the S4R shell element is often used to simulate both thick and thin plates in marine structures (Abaqus/Explicit 2010; Marinatos and Samuelides 2015). The key material properties of the plates in Nurick and Shave (1996) experiments are summarised in Table 5.

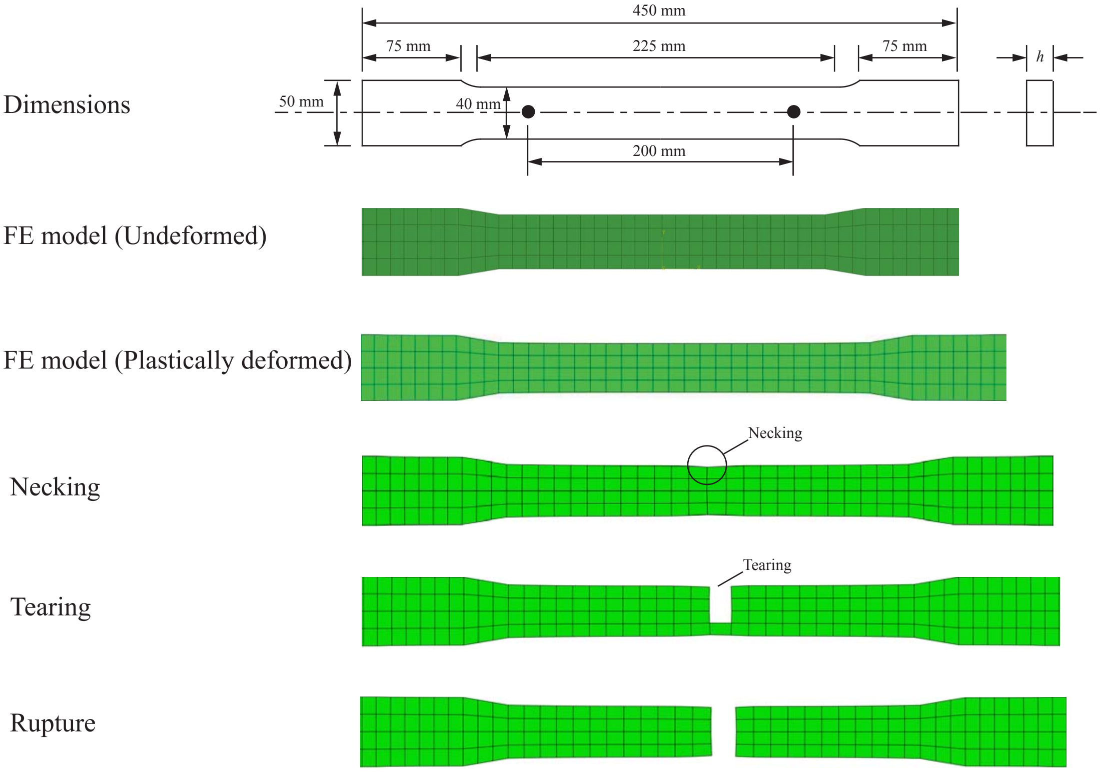

Figure 19. Modelling the uniaxial tensile test – for element size of 10 × 10 × 2.5 mm ($le/h = 2.5$) – to calibrate for the damage parameters.

Table 5. Material properties

Density (ρ)	2830 kg/m^3
Young's modulus (E)	207 GPa
Poisson's ratio (ν)	0.3
Static yield stress (σ_0)	269 MPa
Rupture strain (ε_{rup})	0.31

For each element size ratio l_e/h, the initial strain $\bar{\varepsilon}_d^{pl}$ and the failure strain $\bar{\varepsilon}_f^{pl}$ were calibrated so that the tensile specimen necks at a strain of $\varepsilon = 0.21$ and ruptures at the strain of $\varepsilon_{rup} = 0.31$. The simulated strain-stress curves for different element sizes are shown in Fig. 20.

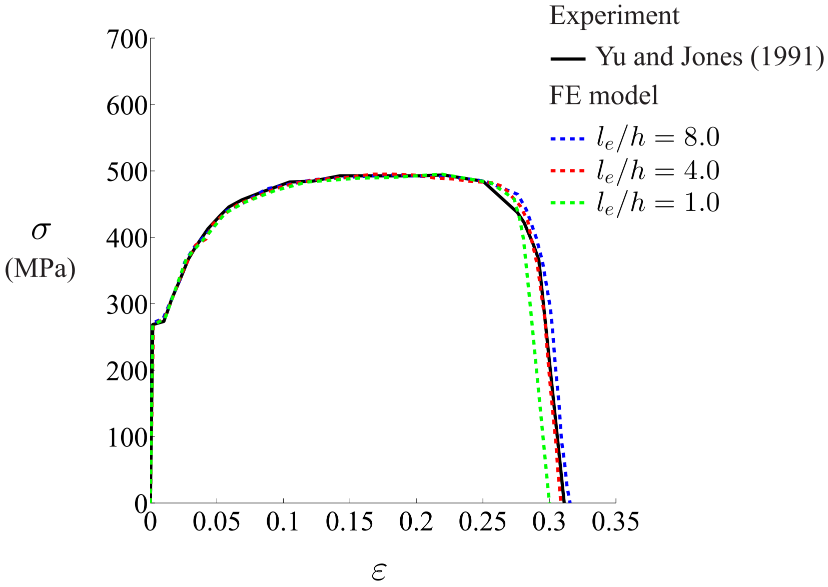

Figure 20. Modelling the uniaxial tensile test with different element size to calibrate for the damage parameters.

Figure 21 shows the calibrated damage parameters for S4R shell element of different size ratio l_e/h. The current results agree with those of Marinatos and Samuelides (2015) where it was found that the values of $\bar{\varepsilon}_d^{pl}$ and $\bar{\varepsilon}_f^{pl}$ reduces with element size ratio l_e/h. It is worth emphasising that, here, the calibration is performed using only strain stress curves obtained from a static uniaxial tensile test. It is unclear how the damage parameters would change under high strain rate loading condition - this remains an active area of research. Due to the lack of material test data for high strain rate conditions, the damage parameters obtained here were used in the simulations to follow.

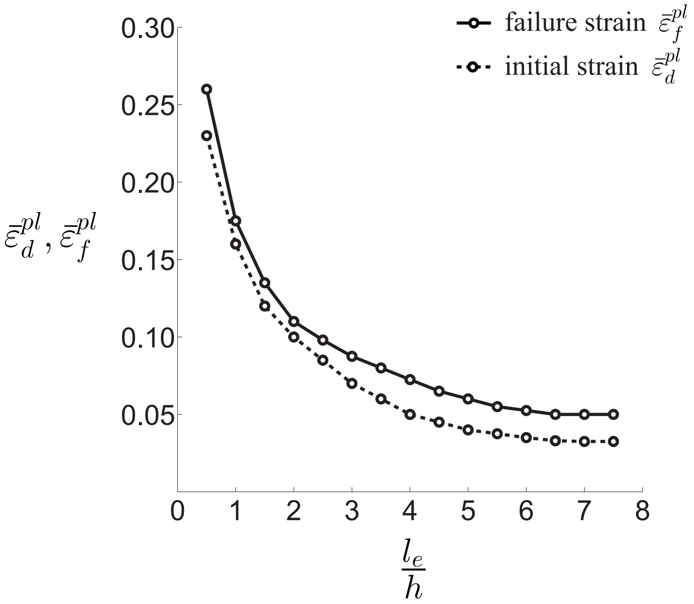

Figure 21. The calibrated damage parameters for S4R shell element for different length/thickness ratios.

4.3. FE model setup

Figure 22 shows a schematic of the FE model for a rectangular plate of length a, width b and thickness h; the aspect ratio of the plate is $\gamma = a/b$ (≥ 1.0). All elements have identical length and width of l_e, and an assigned thickness of h. Due to symmetry, only a quarter of the plate is modelled. Nodes along the plate boundary are fixed in all directions, whereas the nodes on the symmetry lines are given plane symmetric boundary conditions. The applied loading in the model are either impulsive or dynamic. For impulsive loading, an initial velocity is assigned to each element node; for dynamic loading condition, the actual pressure pulse is applied to each element surface.

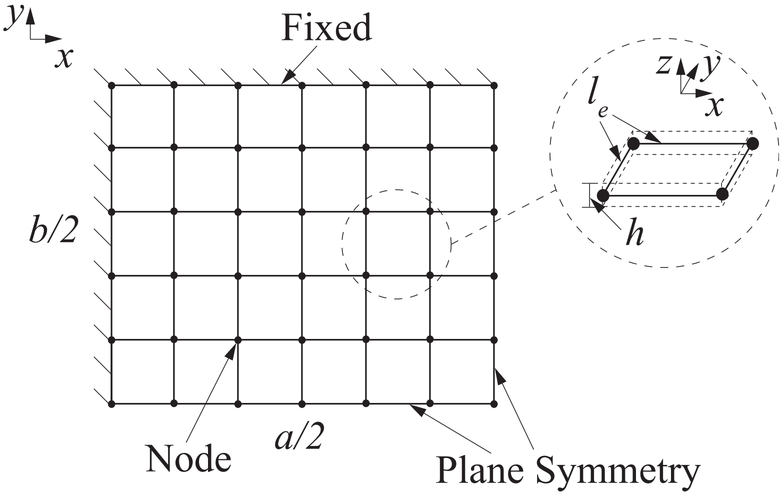

Figure 22. Schematic of the FE model. A quarter of the plate is modelled using *S4R* shell elements. The nodes along the boundary are fixed in all directions, whereas the nodes on other two boundaries are set with plane symmetrical conditions.

A mesh convergence study was first performed to determine the maximum element size ratio l_e/h that would be needed to obtain converged results. To this end, an impulsively-loaded square mild steel plate ($0.089 \times 0.089 \times 0.0016$ m) with element size ratio l_e/h ranging from 0.5 to 7.5 was simulated. Figure 23 plots the state variable Ω and the damage variable Π (for an element located next to the midspan of the plate boundary where incipient material rupture is first expected to occur) against l_e/h where they showed that converged results are reached for $l_e/h < 4$. On the other hand, a plot of the plate central deflection ω_c/h against l_e/h in Fig. 24 shows that converged results are only reached for $l_e/h \leq 2$. Hence, an element size ratio of $l_e/h = 2$ is used, together with damage parameters tabulated in Table 6, throughout. In addition, it must be emphasised that the central deflection ω_c/h also converges to the theoretical prediction by Yu and Chen (1998) when $l_e/h \leq 2$ (see Fig. 24) - this is further confirmation that our choice of element size ratio ($l_e/h = 2$) is appropriate.

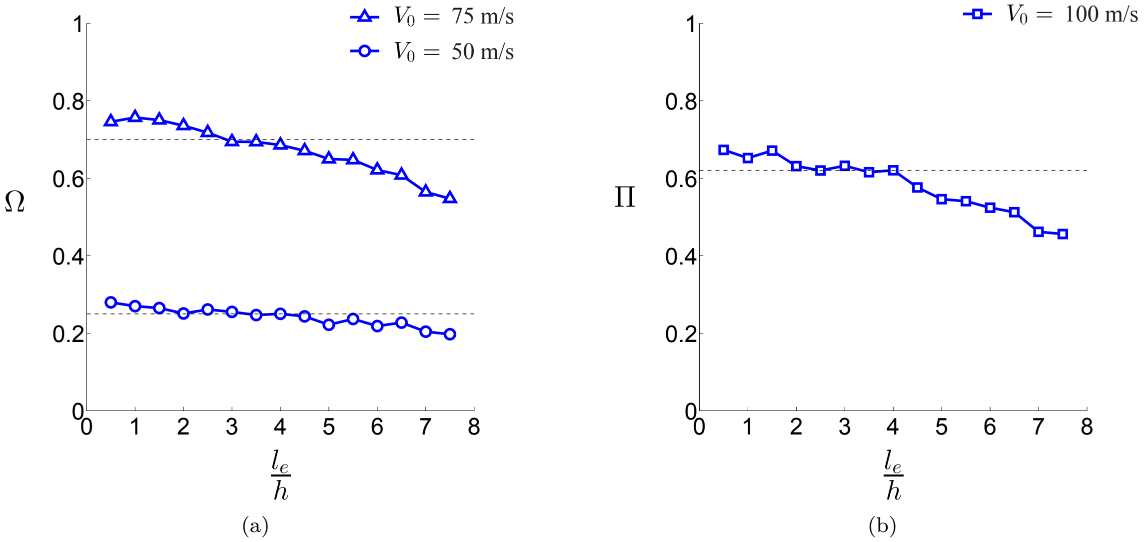

Figure 23. Variations of the state variable Ω and damage variable Π (for an element located next to the midspan of the plate boundary) against element aspect ratio l_e/h at different impulsive velocities (V_0 =50, 75 and 100 m/s).

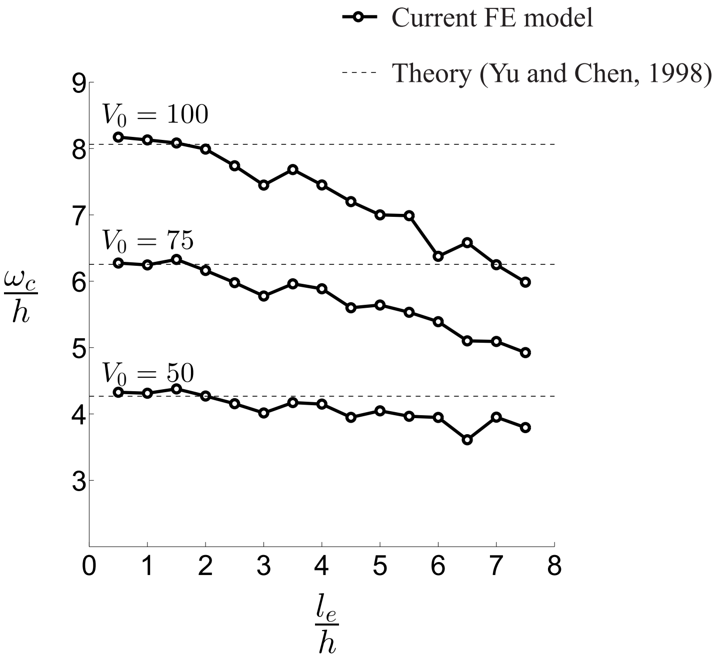

Figure 24. Predicted non-dimensional central plate deflections for different l_e/h. Solid line (–o–o–) is predicted central deflections by FE, and dash line (- - -) is theoretical prediction by Yu and Chen (1998).

Table 6. Damage parameters used in all subsequent FE simulations.

element size ratio l_e/h	initial strain $\bar{\varepsilon}_d^{pl}$	failure strain $\bar{\varepsilon}_f^{pl}$
2.0	0.10	0.11

4.4. Validation

The current FE model is used to predict the onset of mode II failure in a ship plating. First, its predictions must be validated against experimental data by Olson et al. (1993) and Nurick and Shave (1996). It is worth highlighting that the aforementioned experiments used laboratory-scale mild steel plates with dimensions $0.089 \times 0.059 \times 0.0016$ m, where test arrangements were such that specimens were subjected to impulsive loading conditions. Even though these experiments contain data that include all three modes of deformation, only the mode I and mode II data were used to validate the FE predictions for reasons (of maintaining air and water tight integrity) explained in Section 1.

Figure 25 shows the predicted deformation and failure of a mild-steel plate ($0.089 \times 0.059 \times 0.0016$ m) subjected to an impulsive load (corresponding to an initial velocity of $V_0 = 160$ m/s). The plate undergoes large deflection in mode I. As deformation continues, tearing first initiates at the mid-span on the longer edge of the plate boundary – this is always the case – as shown in Fig. 25c. If the blast intensity is sufficiently large, then progressive tearing develops on all sides of the plate boundary, leading eventually to complete detachment from the boundary as shown in Fig. 25d. As soon as tearing initiates, the plate is deemed to have lost its water and air-tight integrity; therefore, preventing the initial tear is critical here.

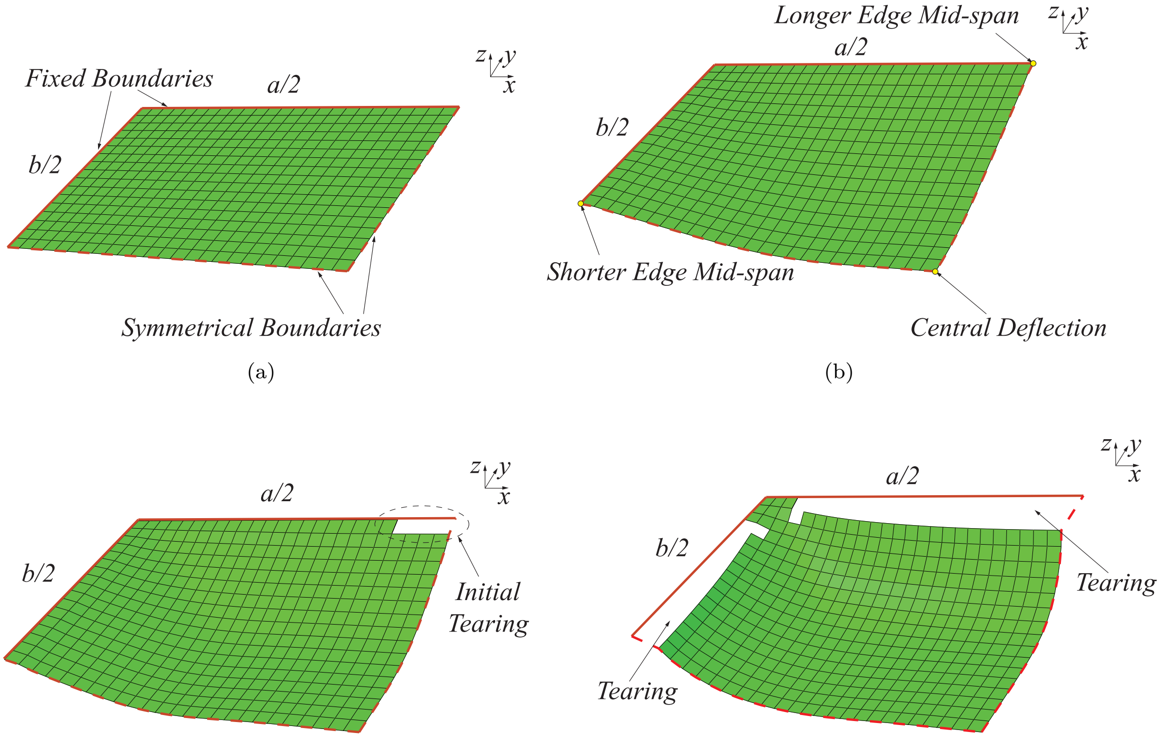

(a) (b) (c) (d)

Figure 25. Predicted deformation and failure of a mild-steel plate ($0.089 \times 0.059 \times 0.0016$ m) subjected to an impulsive load ($V_0 = 160$ m/s): (a) undeformed plate; (b) large inelastic deformation during which the plate maintains air and water-tight integrity; (c) tearing occurs (through material rupture) at mid-span along the longer edge of the plate; (d) tearing progresses along the plate boundary leading to complete detachment from the boundary if the blast is sufficiently intense.

Figure 26 shows a good agreement between the predicted central deflection and experiment. The predicted central deflection increases almost linearly with I^* until the first element is deleted. For the plate dimension shown, the threshold for transition to mode II failure is reached when the dimensionless impulse I^* reaches 0.62 ($V_0 = 107.5$ m/s); at this point, the predicted central deflection is 8.7 times the plate thickness. Interestingly, the central deflection continues to increase with I^* even though tearing had already initiated along its boundary. At some point, large scale tearing leads to a decrease in central deflection as exemplified by a decrease in w_c/h - this is consistent with experimental observations and numerical predictions in literature, see Jones (1997), Rudrapatna et al. (1999) and Yuan and Tan (2013). Since the water- or air-tight capability of plates is of interest here, the threshold for transition to mode II deformation is adopted as the failure criterion (or the limit state). Table 7 compares predicted threshold velocities (for transition to mode II deformation) using the different methods where it can be seen that the current FE model achieves the best accuracy, with a difference of approximately 1.2% compared to experiment.

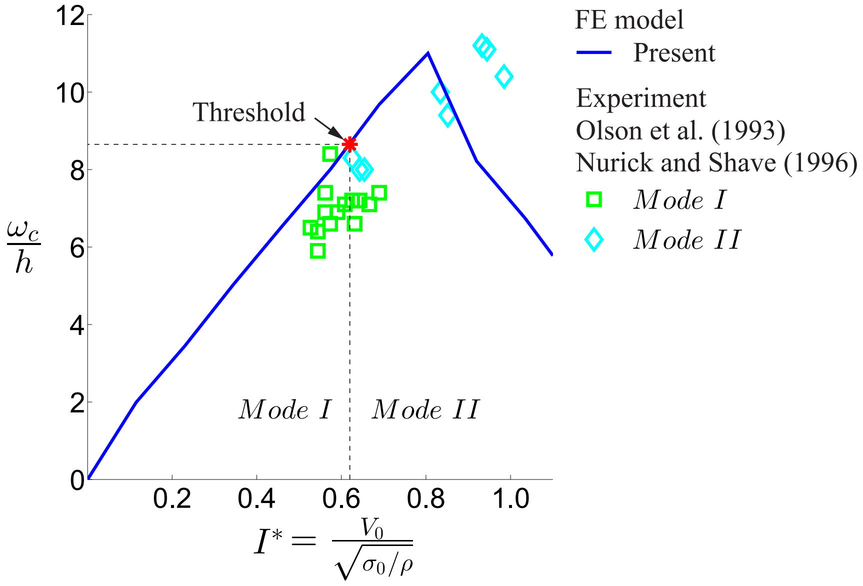

Figure 26. Comparison of predicted central deflections by the FE model to experimental data. All data are obtained from 0.089 × 0.089 × 0.0016 m mild steel plates subjected to increasing impulsive loadings.

Table 7. Threshold velocity for transition to Mode II deformation.

Method	Critical impulse I^*(and velocity V_0 m/s)
Experiment[1]	0.62(108.8)
SDOF [2]	0.73(126.9)
FE	0.62(107.5)
FE[3]	0.75(130.0)
Theory[3]	0.78(135.4)

1:Nurick and Shave (1996), 2: Section 3.4, 3: Yuan and Tan (2013).

5. A case study

5.1. Design conditions

Assuming that a naval ship is to be designed to withstand a far-field air explosion. It has a box-like superstructure of length L which is significantly greater than its height H - see Fig. 2. On the front side of the superstructure, the spacing of the girders and frames are to be 2.0 m ×1.0 m. The outer plating is to be constructed using mild steel which has a static yield stress σ_0 of 237 MPa. The objective is to design a plating needed to maintain air and water tightness for up to an incident overpressure P_i of 5.0 P_0 (507 KPa). The design conditions are summarised in Table 8.

Table 8. Key design parameters

Superstructure Height (H)	11.5 m
Plate length (a)	2.0 m
Plate aspect ratio (γ)	2.0
Static yield stress (σ_0)	237 MPa
Incident pressure (P_i)	507 KPa

Since the design incident pressure P_i is 507 KPa, the blast duration t_p^+ can be obtained from Fig. 3 as 0.155 s. As shown in Fig. 4, the pressure loading is characterised by four parameters P_r, P_s, t_s and t_{p+}, and the first three parameters are calculated using Eqs. 1, 2 and 3. Note that the characteristic dimension of the ship superstructure d_c is the superstructure height H, i.e. $d_c = 11.5$ m. Additionally, the equivalent loading duration t_1 can be calculated using Eq. 4.

Table 9. Parameters of the pressure loading curve

Reflected pressure (P_r)	2280 KPa
Stagnation pressure (P_s)	1034 KPa
blast duration (t_p^+)	0.155 s
Stagnation time (t_s)	0.043 s
Equivalent loading duration t_1	0.095 s

5.2. LRN method

The procedure to design an outer plating of a naval ship superstructure against external blast, as prescribed by Lloyd's Register (2014), is summarised in Fig. 27.

The dynamic load factor f_{DLF} must first be determined before using the scantling equation in Eq. 6. By assuming an initial plate thickness of $h_0 = 5$ mm, the value of the f_{DLF} is determined from Fig. 5. In this design case study, the material hardening factor f_σ is 1.3 and the plate aspect ratio factor f_γ is 750. Using the aforesaid information, the plating thickness h is calculated using Eq. 6. Before obtaining the final plating thickness, several iterations are needed in order to obtain a converged value for f_{DLF}. Figure 28 shows how f_{DLF} and h changes with number of iterations N.

Figure 28b shows that the converged plating thickness is 43 mm. Therefore, a mild steel plating of dimensions 2000 mm ×1000 mm ×43 mm is sufficient to resist (maintain air

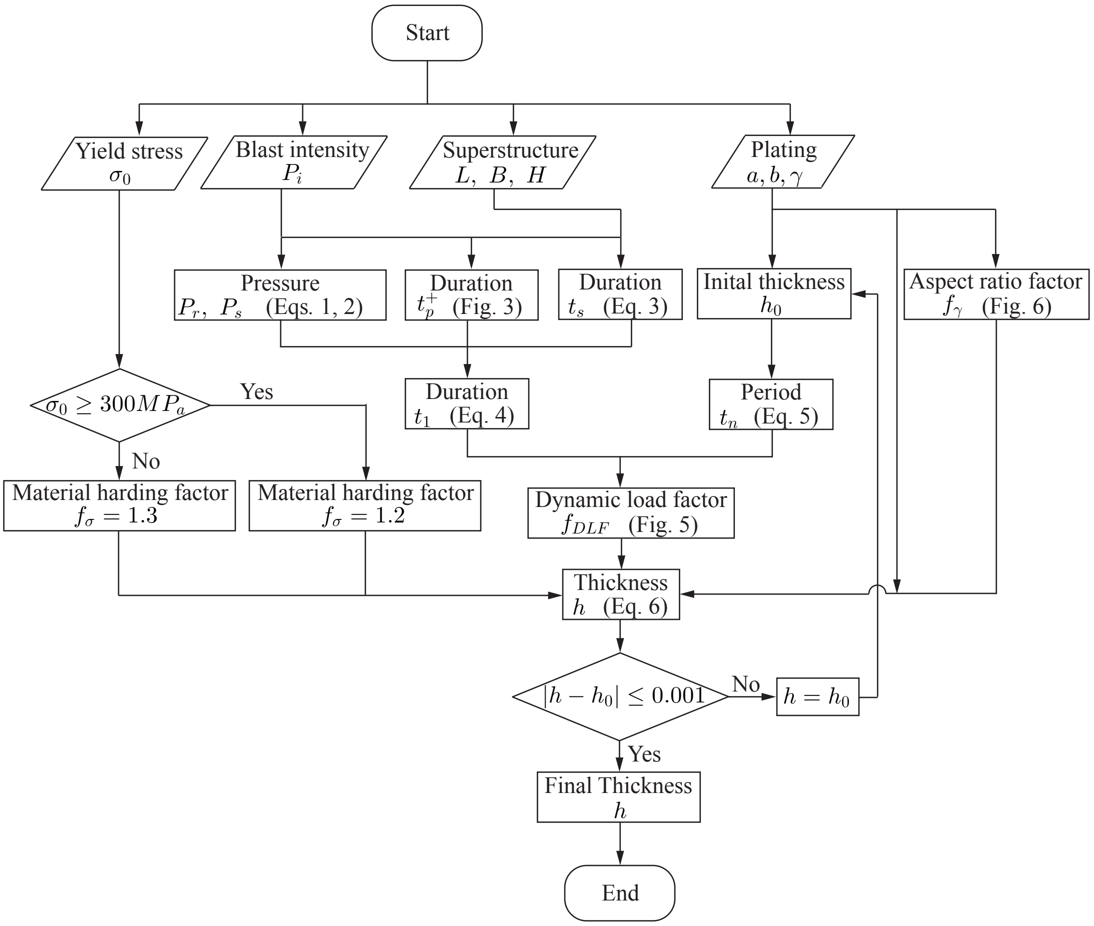

Figure 27. Flow chart of design procedure for external blast by Lloyd's Register (2014).

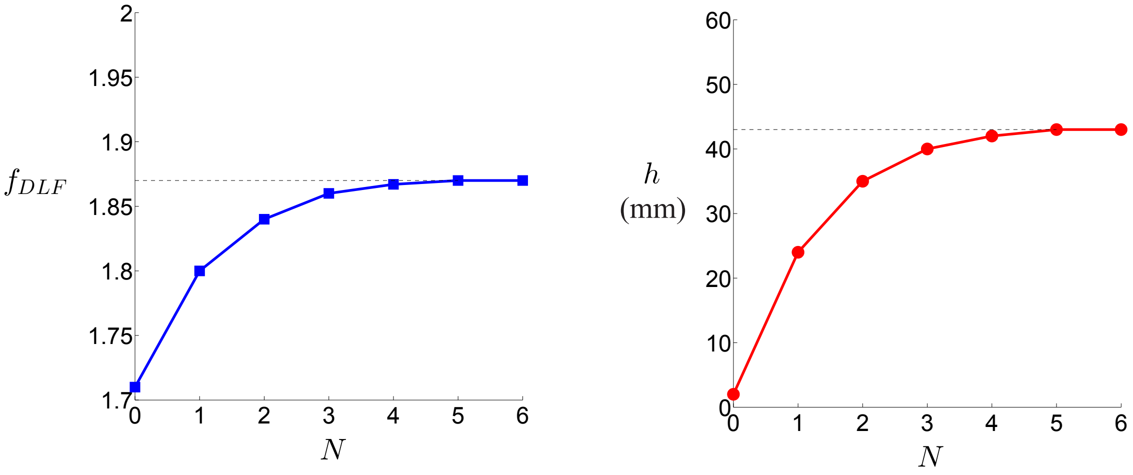

(a)

(b)

Figure 28. Variations of the dynamic load factors f_{DLF} (a) and plating thicknesses h (b) with the number of iterations N.

and water tightness) an external blast with an incident pressure of $5P_0$ according to LRN.

5.3. SDOF method

Figure 29 shows a flow chart of the key steps when designing a ship plating. The primary objective is to determine the minimum thickness of a plating such that it is at the threshold of model II failure under the given loading condition.

Following the flow chart in Fig. 29, a plating thickness of 45.0 mm is initially assumed. The increment for each iterations is set as follows: $\Delta t = 0.01$ ms and $\Delta h = 0.1$ mm. In every iteration, the central deflection over time is recorded. Figure 30 shows the deflection curves for the platings with thicknesses as 25, 30 and 35 mm, respectively. The maximum deflection in each curve corresponds to the first peak value - this is a direct consequence of the decreasing loading pressure. It is evident that the predicted maximum central deflection generally increases with a reduction of the plating thickness. Therefore, the maximum tensile strain calculated by Eq. 39 would also increase accordingly.

Figure 31 shows a general increase of the maximum tensile strain ε_{max} as the plating thickness reduces. When the value of ε_{max} reaches the material rupture strain ε_{rup}, the iteration is terminated. Therefore, the final plating thickness, needed to ensure air and water-tight integrity, is 17.5 mm according to the SDOF model.

5.4. FE method

Figure 32 presents a flow chart that shows how the current FE model is used to design a ship plating. The key is to search for deleted element in the output file.

An initial plating thickness of 40.0 mm was chosen and this was reduced by $\Delta h = 0.1$ mm for each iteration. Figure 33 shows the variation of maximum damage variable Π for an element located at mid-side of the plate model - this is the first element deleted from the mesh. When the value of Π reaches 1.0, the element deletion occurs. The final plating thickness is 12.2 mm, according to the FE model. The predictions by the three methods are summarised in Table 10.

Table 10. Predictions of plating thickness.

plating thickness	LRN	SDOF	FE
h (mm)	43.0	17.5	12.2

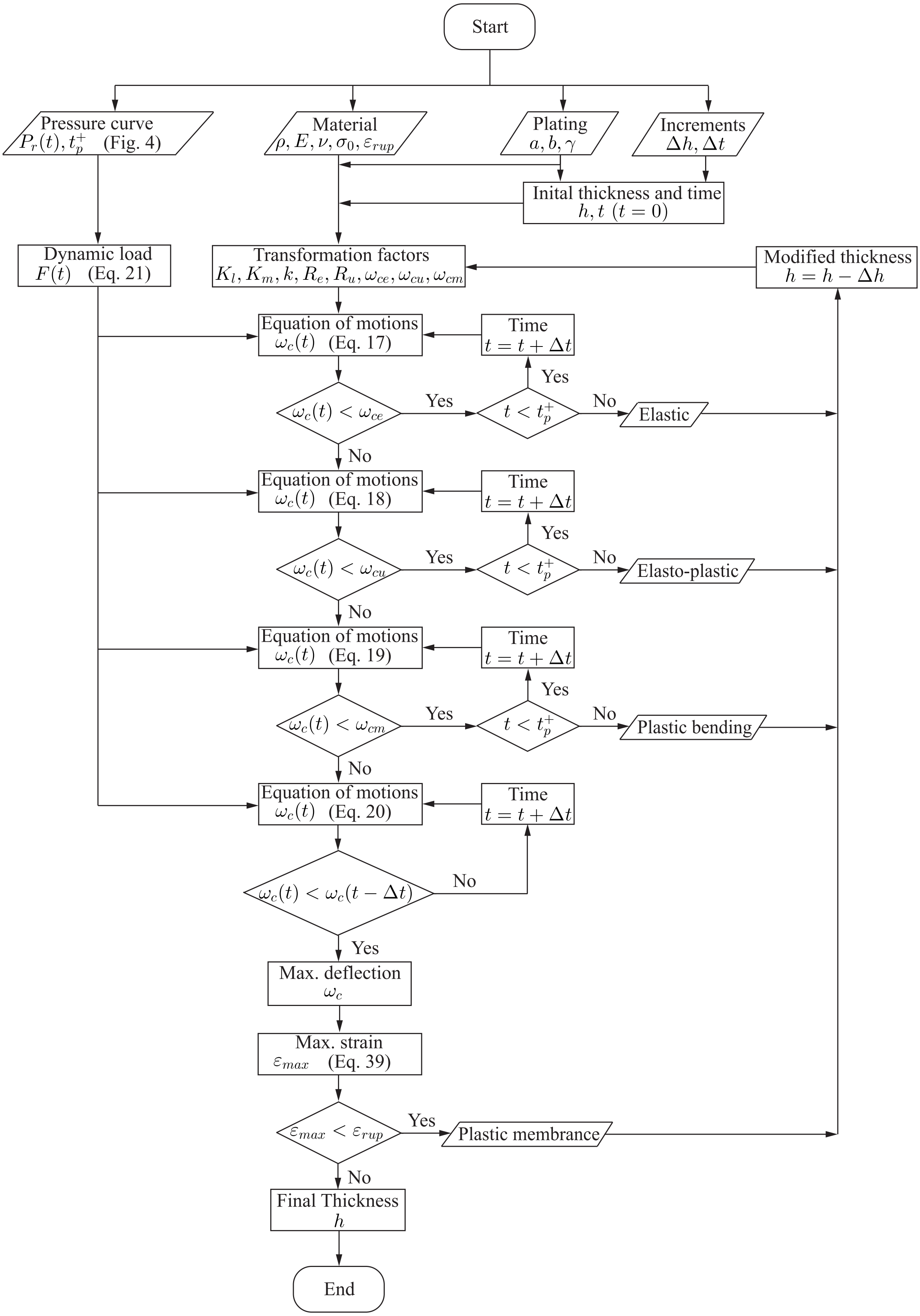

Figure 29. Flow chart on using the SDOF model to design a ship plating against external blast.

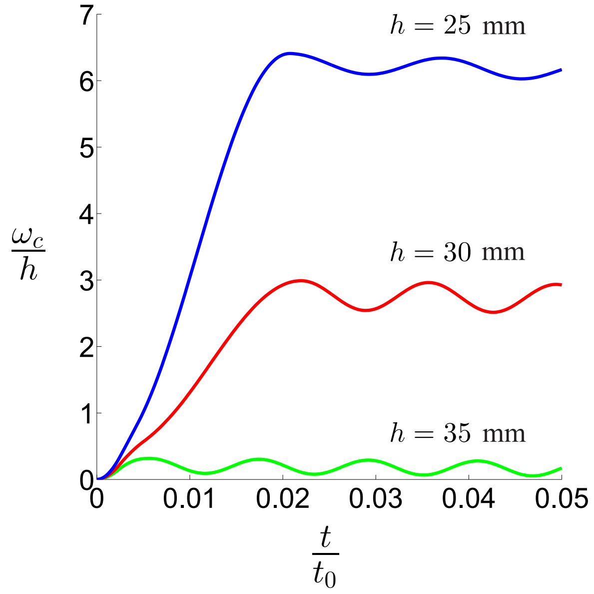

Figure 30. Central deflection of platings with different thickness subjected to an identical bilinear pulse loading shown in Fig. 4. Note that t_0 is the standard loading duration of 0.4 s.

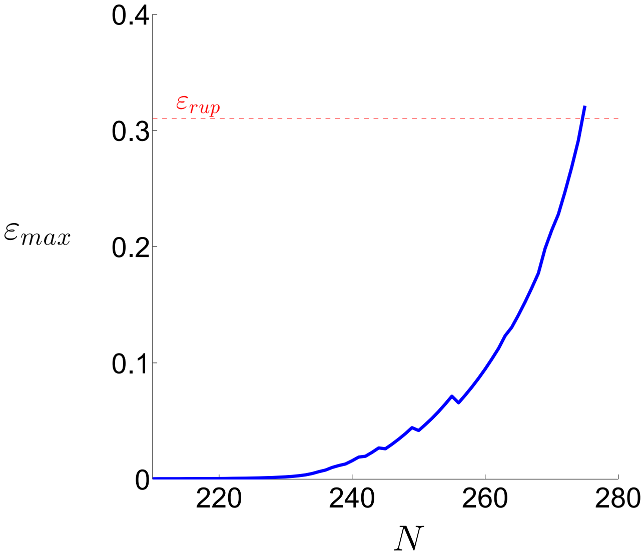

Figure 31. The increment of tensile strain ε_{max} in the plating against number of iterations N.

6. Results and discussions

6.1. Design conditions

To interrogate the accuracy, and provide a rationalisation, of the philosophy behind the design equation (Eq. 6), it is necessary to compare the plating thicknesses (stipulated by LRN) to that predicted by the SDOF and FE models for a broad range of possible design conditions. The plate dimensions must cover nearly all the conceivable geometric

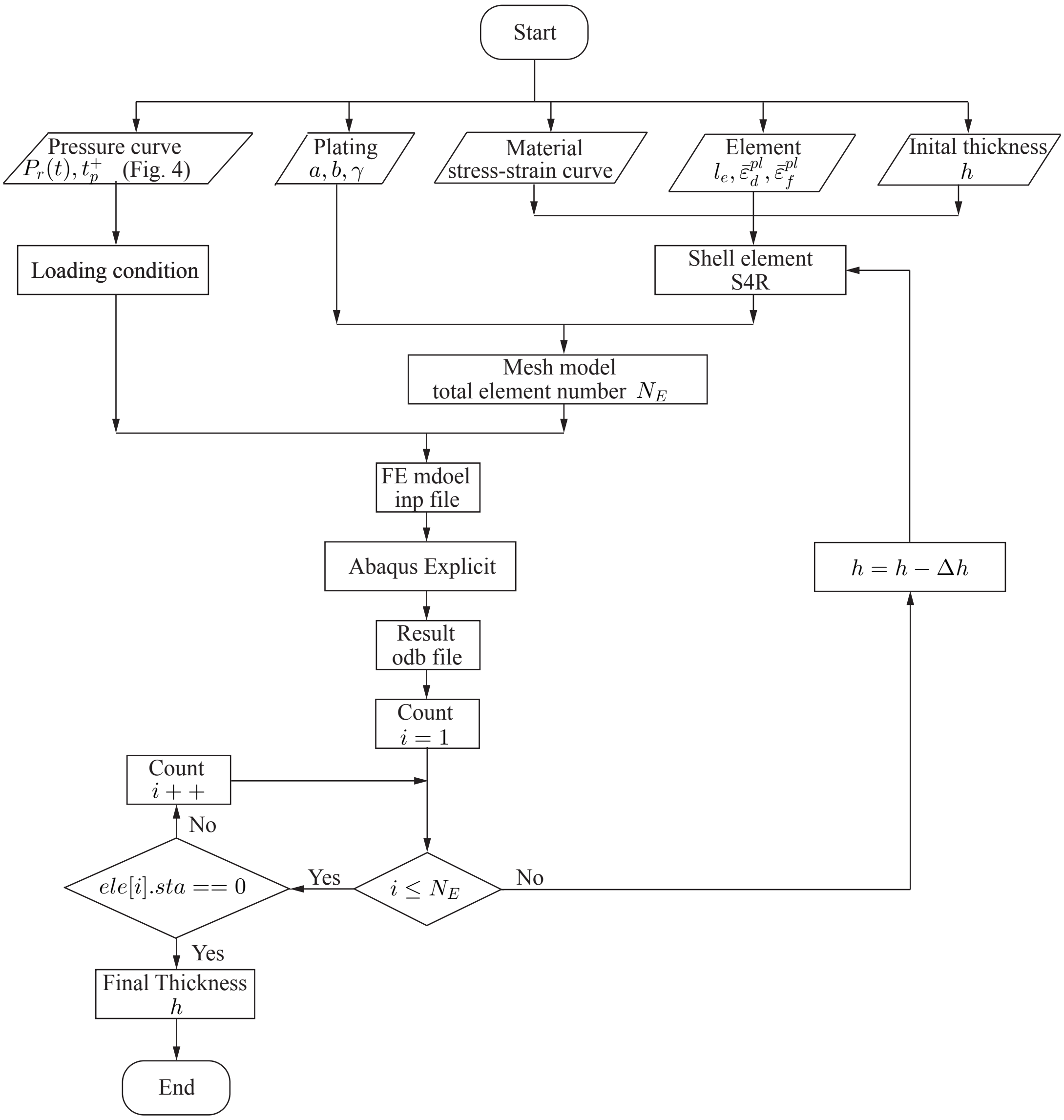

Figure 32. Flow chart on using the validated FE model to design a ship plating against external blasts.

combinations that might be used to construct a naval ship superstructure. Similarly, an extensive range of external blast intensities must also be considered in the assessment.

6.1.1. Geometric and material properties of the platings

The platings of a naval ship superstructure are determined by the arrangements of its underlying primary structure. Based on the allowable frame and girder spacings by Lloyd's Register (2013), the upper and lower bound for the plating length a is 0.5 m and 3.0 m, respectively. The aspect ratio γ of an un-stiffened rectangular plating typically ranges between 1.0 to 4.0 and, again, this is stipulated by Lloyd's Register (2014). Table 11 summarises the different combination of plate dimensions that will be considered in this study.

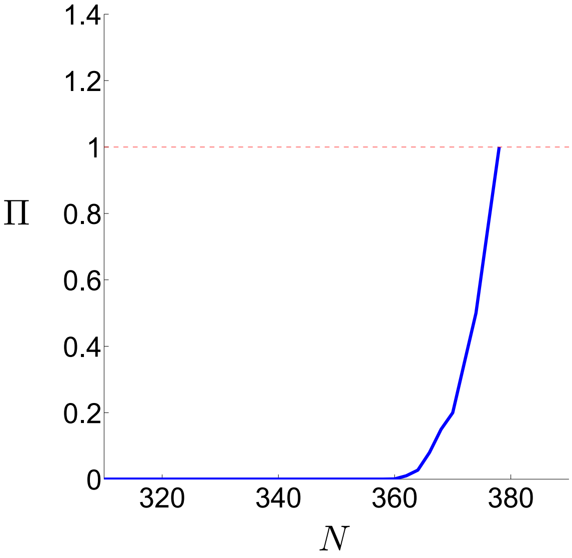

Figure 33. Variation of the maximum damage variable Π for an element located at mid-side of the plate model - this is the first element deleted from the mesh. The number of iterations were indicated by N.

Table 11. Combination of plate dimensions to be considered.

Length (a), m	Aspect Ratio (γ)	Area (A), m^2
0.5	1.0	0.250
0.5	2.0	0.125
0.5	3.0	0.083
0.5	4.0	0.063
3.0	1.0	9.000
3.0	2.0	4.500
3.0	3.0	3.000
3.0	4.0	2.250

Another important parameter in design is the choice of plate material. In the present study, a marine Grade A mild steel was chosen since this is commonly used in marine structures and has one of the lowest yield stress σ_0 according to the certification of materials in Lloyd's Register (2014). Table 12 gives the properties of the mild-steel plate. Additionally, in the FE models, the damage parameters are identical to those calibrated in Sections 4.3.

Table 12. Material properties: Mild steel

Density (ρ)	7830 kg/m^3
Young's modulus (E)	197 GPa
Static yield stress (σ_0)	237 MPa
Poisson's ratio (ν)	0.3
Rupture strain (ε_{rup})	0.31

6.1.2. Range of blast loadings

Lloyd's Register (2014) did not provide a range of loading to be considered for design, and nearly all previous studies (Dye and Lankford 1966; Dow 1994) were limited to low intensity incident pressures where P_i is less than 1.0 P_0 (atmospheric pressure). In this study, the Lloyds' Register design procedure will be assessed for a range of P_i between 0.5 P_0 and 8.0 P_0. In this range, the incident pressure is representative of a navy ship subjected to a 1 *kilotonne* TNT at the standoff distance of between 50 to 400 m, according to LRN. The positive blast duration (t_p^+) also corresponds to a 1 *kilotonne* TNT blast as stipulated by LRN. Another important consideration is the stagnation point of the pressure pulse - this is affected by the dimensions of the superstructure. As indicated in Eq. 3, the time (t_s) to reach stagnation is proportional to the height of the superstructure H (see Fig. 34). Two limiting superstructure heights H, based on the plating dimensions and the incident blast parameters, were considered here, viz. 2 H_s (4.6 m) and 8 H_s (18.4 m) where H_s is the standard superstructure height (2.3 m) as suggested by the International Maritime Organization (1966/1988). These two heights provide sufficient frontal surface area of up to a maximum size of 3.0 × 3.0 m (Table 11); whilst, also, ensuring that the stagnation point of the pressure pulse would, in the worst case, give rise to a triangular pulse ($P_r t_p^+$ in Fig. 34) for the entire range of incident pressures.

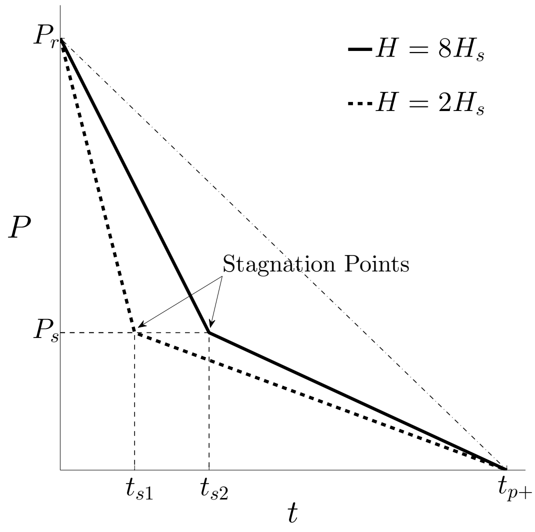

Figure 34. Pressure pulses used in the present study, where H_s (=2.3 m) is the standard superstructure height in accordance to the International Maritime Organization (1966/1988).

Once P_i is assigned, all the other blast parameters in Fig. 34 can be calculated using the LRN procedure described in Section 2.1. A summary of the design blast parameters to be considered is plotted in Fig. 35.

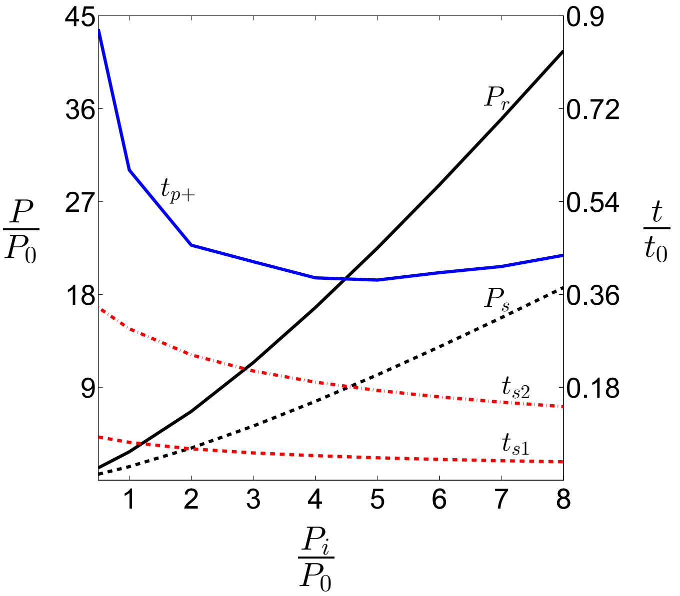

Figure 35. Blast parameter curves for $P_0 = 101.3\ KP_a$ and $t_0 = 0.4\ s$

6.2. *Method and results*

6.2.1. *Design requirement by LRN*

Figure 36 plots the results for the non-dimensional thicknesses h/a against loading intensities P_i/P_0 for a range of plate aspect ratios γ.

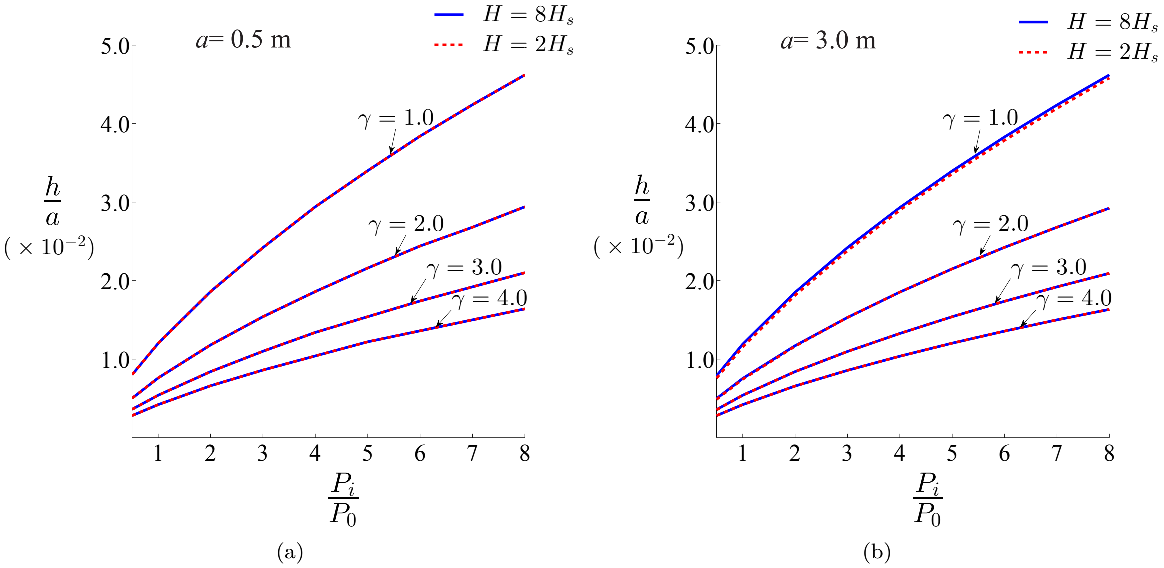

(a)

(b)

Figure 36. Design plating thickness by LRN: (a) plating length a of 0.500 m ; (b) plating length a of 3 m, where the dash lines for $H = 2\ H_s$ and the solid lines for $H = 8\ H_s$.

Figure 36a plots the design thickness h, following the LRN, for a plating of length

$a = 0.5$ m. It is worth highlighting that the curves for $H = 8\ H_s$ and $H = 2\ H_s$ overlap each other for the entire range of aspect ratios. The same is also observed in Fig. 36b for the 3.0 m plating, with the exception of $\gamma = 1.0$ where there is a maximum difference of up to 4.0% at $P_i = 0.4P_0$. These overlaps in the calculated thickness reveal that the height of the superstructure – it affects the stagnation point in the pressure pulse – has a negligible effect on the final plating thickness in design. This is because the positive duration t_p^+ (> 0.15 s in the present study) of the external blast pulse is, at least, an order of magnitude greater than the natural period of vibration by the plate t_n (< 0.07 s). From Eqs. 1-4 and Fig. 5, the dynamic load factors f_{DLF} have a nearly constant value of $f_{DLF} \approx 1.856$. Consequently, the predicted thickness by Eq. 6 in insensitive to the position of the stagnation point in the blast pulse.

6.2.2. SDOF approach

Figure 37 shows the predicted thickness for plating of length $a = 0.5$ m and 3.0 m, with an aspect ratio γ ranging between 1.0 and 4.0.

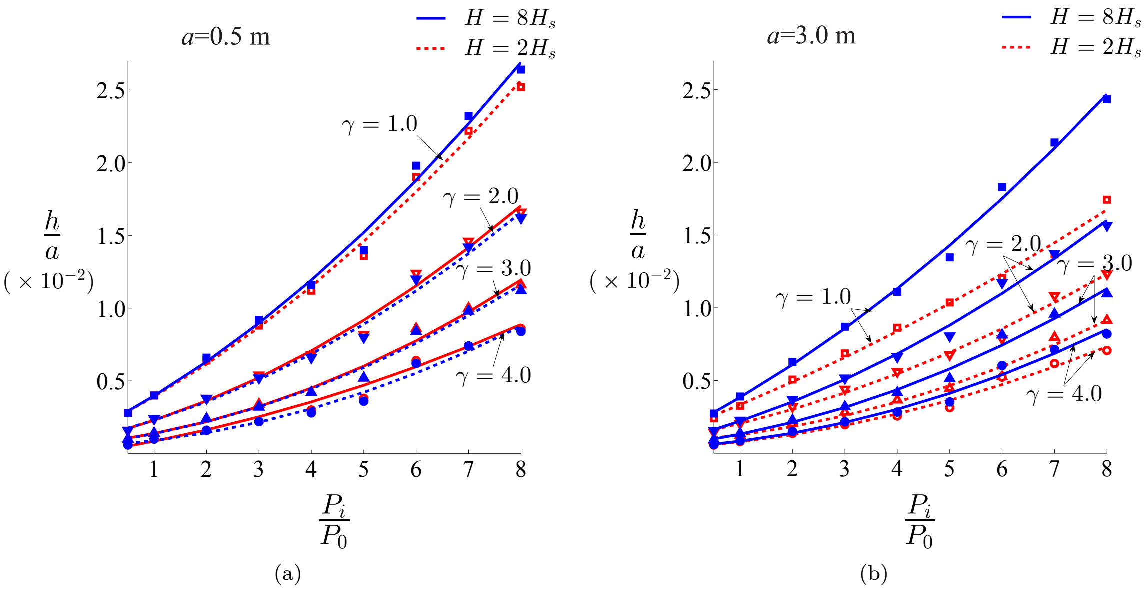

Figure 37. Predicted non-dimensional thickness by the SDOF method for plating length a of (a) 0.5 m and (b) 3.0 m. Solid markers are points for $H = 8\ H_s$ and hollow markers are points for $H = 2\ H_s$. The solid and dash lines are best fit curves of the predicted results.

In Fig. 37, the predicted results for $H = 8\ H_s$ and $H = 2\ H_s$ are indicated by solid and hollow markers, respectively. Second-order trend-lines were also fitted to each of the aforesaid data set for better visualisation of the variations of h/a with loading intensity P_i/P_0. For a small plating $a = 0.5$ m, see Fig. 37a, the difference between the two trend-lines is negligible for all γ; by contrast, their difference increases significantly for the larger plating of $a = 3.0$ m in Fig. 37b. The difference is particularly evident when the plate area is large, see for example $a = 3.0$ m and $\gamma = 1.0$. The significant increase in differences, as seen in Fig. 37b, are due to predictions by Eq. 20 in the plastic membrane phase. As is evident from Eq. 20, the predicted central deflection ω_c is affected by the equivalent natural period t_n^{IV} $(=2\pi\sqrt{\frac{K_m^{\mathrm{IV}}M}{K_l^{\mathrm{IV}}k^{\mathrm{IV}}}})$ and the stagnation time t_s. From Table 1, it can be seen that the natural period t_n^{IV} is effected by the plating length a since $t_n^{IV} = 2\pi a\sqrt{\frac{K_m^{\mathrm{IV}}\rho}{K_l^{\mathrm{IV}}\gamma\sigma_0}}$. Given a plate of length $a = 3.0$ m, aspect ratio $\gamma = 1.0$ and thicknesses $h = 0.01$ m, the equivalent natural period t_n^{IV} is, therefore, 0.042 s. At $P_i = 8.0P_0$, the stagnation time t_s are $t_{s1} = 0.014$ s and $t_{s2} = 0.057$ for $H = 2H_s$ and $H = 8H_s$, respectively (Fig. 35). Since $t_{s1} < t_n^{IV} < t_{s2}$, the central deflection ω_c predicted by Eq. 16 will differ significantly for superstructures of different height H. By contrast, if the plate has a length of 0.5 m, the equivalent natural periods t_n^{IV} are much smaller compared to the stagnation times t_s, and the predicted central deflections ω_c are, consequently, less sensitive to changes in H. The differences in predicted central deflections ω_c would further contribute to differences in final plating thicknesses h according the failure criterion Eq. 40.

6.2.3. FE approach

Figure 38 plots the predicted non-dimensional thickness, where the symbols and lines have the same meaning as that used in Fig. 38.

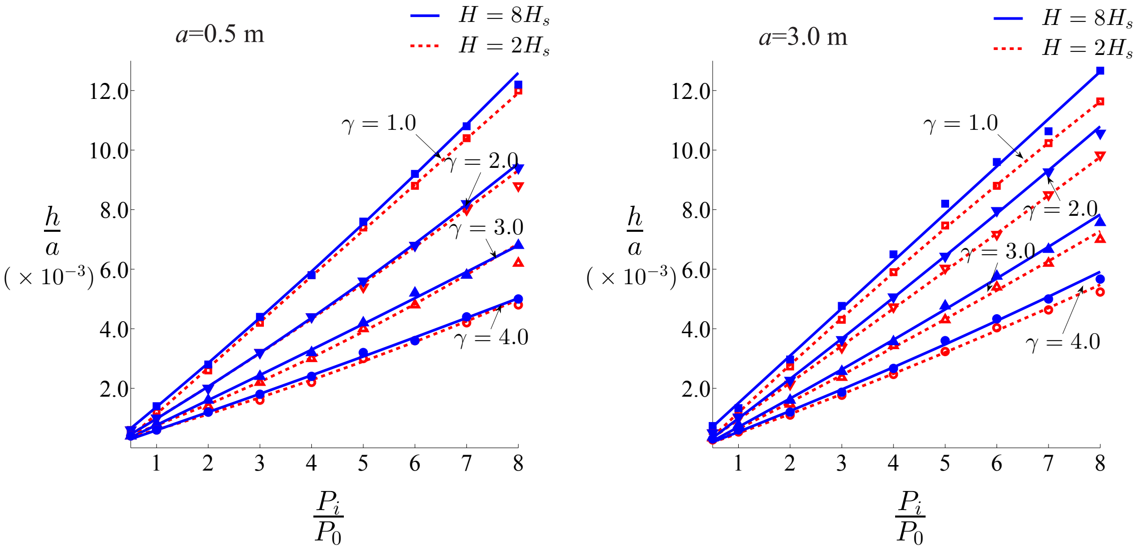

(a) (b)

Figure 38. Design plating thicknesses predicted by FE for plating length a of (a) 0.5 m and (b) 3 m. Solid markers are points for $H = 8\ H_s$ and hollow markers are points for $H = 2\ H_s$. The solid and dash lines are best fit curves of the predicted results.

Figure 38 shows that h/a increases almost linearly with loading intensity P_i/P_0. The differences between $8H_s$ and $2H_s$ are greater for the larger plating ($a = 3.0$ m) compared to the smaller one ($a = 0.5$ m). This is likely a consequence of the time t_{cmax} it takes for a plate to reach its maximum deflection ω_{cmax}. In general, the larger plate ($a = 3.0$ m) have a much longer t_{cmax} than its smaller counterpart ($a = 0.5$ m); consequently, changes in the pressure pulse (Fig. 34) because of the different superstructure heights H would have a greater influence upon the predicted final thickness of the larger plate.

6.3. Failure map and comparison of predictions

It is evident through comparison of the non-dimensional thickness in Figs. 36, 37 and 38 that the FE model predicts the smallest thickness of the three approaches. Under certain design conditions (plating length $a = 3.0$ m, aspect ratio $\gamma = 1.0$), the thickness predicted by FE is nearly 75% less than that calculated using Eq. 6. The discrepancies between the three approaches are due to the different criteria used to determine failure of the plating: LRN uses the ultimate resistance R_u (Section 2.2); whereas, both the SDOF and FE models are based on the criterion of incipient material rupture at the support. Predictions by the SDOF are, in general, higher than those by FE. One reason is that the former adopts a separated four-phases deformation, each with its own equation of motion (Eqs. 17, 18, 19 and 20) to simulate deformation; hence, the max central deflection ω_{cmax} and the time taken to reach maximum deflection t_{cmax} are larger than those obtained by direct calculations using FE. The longer time needed to reach maximum deflection t_{cmax} also makes the SDOF model (see Fig. 37) more sensitive to changes in the stagnation point of the pressure pulse. Another reason for the higher SDOF predictions, compared to FE, is that the latter takes into account material strain hardening and strain-rate effects, unlike in the former. It must be emphasised that to properly consider the effects of strain rate, a methodology must be developed to determine the strain-rate $\dot{\varepsilon}$ at every time increment - this is difficult to accurately obtain in a SDOF approximation. However, to examine its effects upon the SDOF prediction, we follow the procedure outlined in Lloyd's Register (2014) by employing a material hardening factor f_σ to increase the static yield stress σ_0. Figure 39 shows how the differences between SDOF and FE predictions reduce with increasing dynamic yield stress of $\sigma_d = 1.5\sigma_0$ and $\sigma_d = 2.0\sigma_0$, they correspond to a nominal strain rate of 266.4 s^{-1} and 1252.4 s^{-1} according to Eq. 47.

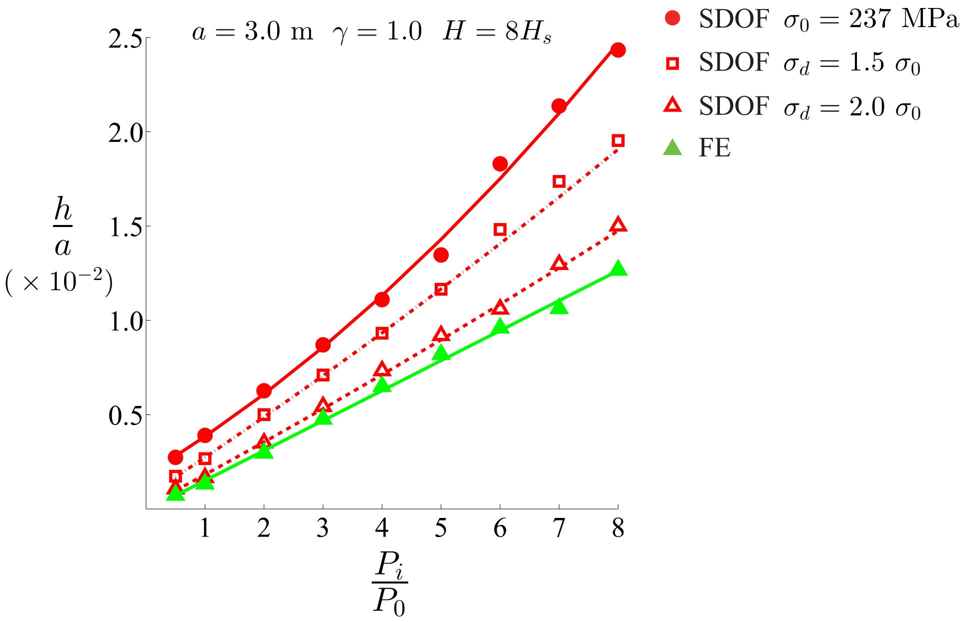

Figure 39. Comparison of predicted thicknesses by FE against those by the current SDOF model for elevated yield stress due to material strain rate effects.

A failure map is plotted in Fig. 40 to compare the aforesaid predictions. Dimensionless parameter P_i/P_0, h/a and γ were previously used to plot Figs. 36 - 38. Since P_0 (atmospheric pressure) is common to all the figures, it can be replaced by the static yield stress σ_0 of the plating material. Defining $m_0 = \sigma_0 h^2/4$ as the unit plastic moment of a plate, the failure map can now be characterised by just two parameters: a dimensionless load $P_i a^2/m_0$ and aspect ratio γ. The predicted thickness shown in the various figures in Section 5.3 can now be replotted in Fig. 40 below.

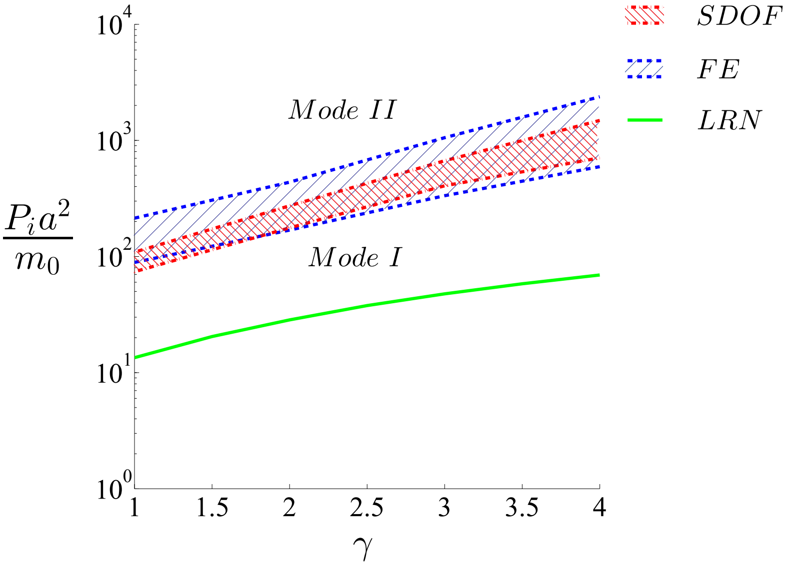

Figure 40. Failure map comparing the predictions by the different approaches. $m_0 = \sigma_0 h^2/4$ is unit plastic moment of the plate.

Notice that predictions by the LRN method collapses onto a single curve which is in contrast to that obtained by SDOF and FE. To understand why this is the case, Eq. 6 is re-arranged in the following form:

$$\frac{h}{a} = \sqrt{\frac{f_{DLF} P_r}{6 f_\sigma \sigma_0 \gamma (1 + \frac{f_\gamma}{1000}\gamma)}} \tag{48}$$

where P_r is peak pressure, σ_0 is the static yield stress with its coefficient f_{σ_0}, plating aspect ratio γ with its coefficient f_γ, and dynamic loading factor f_{DLF}. Since the peak pressure P_r depends only on the incident pressure P_i (Eq. 1), then for any set of design condition (P_i and σ_0 are selected) the only variable is f_{DLF}. In an external blast scenario, the loading duration t_p^+ is much longer than the natural period of a plating t_n; consequently, the values of the f_{DLF} are almost a constant ($f_{DLF} \approx 1.870$). Therefore, the dimensionless load $P_i a^2/m_0$ depends only on the plating aspect ratio γ for the LRN results.

In contrast, predictions by the SDOF and FE exhibit a broad distribution in Fig. 40. To explain this, notice that at an aspect ratio of $\gamma = 2.0$, the dimensionless load $P_i a^2/m_0$ predicted by FE model can vary from 168.9 to 436.3. Consequently, predictions by SDOF and FE yield a range of dimensionless load $P_i a^2/m_0$ when plotted against plate aspect ratio γ. Since the SDOF and FE models were designed to prevent mode II failure, the lower of the two boundaries could be regarded as the limit for mode I failure. Below the boundaries, a plating only exhibits large plastic deformation, i.e. tearing does not initiate. This also suggests that a plating design using the Lloyd's Register design procedure will achieve the purpose of maintaining water or gas-tight integrity; however, the calculated thickness contains unnecessary redundancy and is overly conservative (by up to 50% greater than the minimum thickness needed to maintain water and gas tight integrity).

7. Conclusion

This paper assesses and provides a rationalisation of the different approaches for designing superstructure platings against external blasts. The Lloyd's Register (2014) design procedure is carefully analysed. A new 4-phase SDOF model is developed to predict the large plastic behaviour of plates, and a FE model using shell elements is developed to capture in greater detail the dynamic behaviour of the platings. These methods were evaluated for a broad range of design conditions. The present work reveals certain limitations in understanding the blast loading mechanisms such as the loading curve effected by the superstructure dimension. Moreover, dynamic response of common used stiffened panels analysis and the interaction between fluid and structure still need further work.

8. Acknowledgement

The authors are grateful to Dr Colin Morison of TPS Consult (UK), and to Paul James and Dimitrios Chalas from Lloyd's Register for the invaluable discussions. Financial support from the Ministry of Defence, UK (David Manley - DE&S Sea Systems Group) and QinetiQ (Robert Ball - Structures & Survivability, Platform Design and Life Support IDT) is gratefully acknowledged.

References

Abaqus/Explicit, 2010. Abaqus/Explicit: User's Manual.
Biggs, J. M., 1964. Introduction to Structural Dynamics. McGraw-Hill New York.
Dechaumphai, P., Wansophark, N., 2011. Numerical Methods in Engineering: Theories with MATLAB, Fortran, C and Pascal Programs. Alpha Science International.
Det Norske Veritas, 2010. Design against Accidental Loads.
Dow, R. S., 1994. Experimental and theoretical response prediction of steel-stiffened glass-reinforced plastic ship deckhouse subject to blast loading. Mar. Struct. 7 (2), 399–416.
Dunne, F., Petrinic, N., 2005. Introduction to computational plasticity. Oxford University Press.
Dye, L. C., Lankford, B. W., 1966. A simplified method of designing ship structure for air blast. Nav. Eng. J. 78 (4), 693–701.
Ehlers, S., Broekhuijsen, J., Alsos, H. S., Biehl, F., Tabri, K., 2008. Simulating the collision response of ship side structures: a failure criteria benchmark study. Int. Shipbuild. Prog. 55 (1), 127.
Fagnan, J. R., 1996. Failure analysis of stiffened and unstiffened mild steel plates subjected to blast loading. Ph.D. thesis, University of British Columbia.
Germanischer Lloyd, 2012. Rules for Classification and Construction.

Houlston, R., Slater, J., Pegg, N., et al., 1985. On analysis of structural response of ship panels subjected to air blast loading. Comput. Struct. 21 (1-2), 273–289.

International Maritime Organization, 1966/1988. International Convention on Load Lines.

Jones, N., 1997. Dynamic inelastic failure of structures. Trans. of the Japan Soc. of Mech. Engrs. Series A 63 (616), 2485–2495.

Jones, N., 2011. Structural Impact. Cambridge University Press.

Lloyd's Register, 2013. Rules and Regulations for the Classification of Ships.

Lloyd's Register, 2014. Rules and Regulations for the Classification of Naval Ships.

Marinatos, J. N., Samuelides, M. S., 2015. Towards a unified methodology for the simulation of rupture in collision and grounding of ships. Mar. Struct. 42, 1–32.

Morison, C. M., 2006. Dynamic response of walls and slabs by single-degree-of-freedom analysis - critical review and revision. Int. J. Impact Eng. 32 (8), 1214–1247.

Nurick, G. N., Shave, G. C., 1996. The deformation and tearing of thin square plates subjected to impulsive loads- experimental study. Int. J. Impact Eng. 18 (1), 99–116.

Olson, M. D., Nurick, G. N., Fagnan, J. R., 1993. Deformation and rupture of blast loaded square plates-predictions and experiments. Int. J. Impact Eng. 13 (2), 279–291.

Pavlovic, M., Markovic, Z., Veljkovic, M., Budevac, D., 2013. Bolted shear connectors vs. headed studs behaviour in push-out tests. J. Constr. Steel Res. 88, 134 – 149.
URL `http://www.sciencedirect.com/science/article/pii/S0143974X13001314`

Registro Italiano Navale, 2011. Rules for the Classification of Naval Ships.

Rudrapatna, N. S., Vaziri, R., Olson, M. D., 1999. Deformation and failure of blast-loaded square plates. Int. J. Impact Eng. 22 (4), 449–467.

Smith, P. D., Hetherington, J. G., 1994. Blast and Ballistic Loading of Structures. Butterworth Heinemann.

Stronge, W. J., Yu, T. X., 1995. Dynamic Models for Structural Plasticity. Springer Science & Business Media.

Timoshenko, S., Woinowsky-Krieger, S., 1959. Theory of Plates and Shells. Vol. 2. McGraw-hill New York.

US Army Corps of Engineers, 1957a. Design of Structures to Resist the Effects of Atomic Weapons – Principals of Dynamic Analysis and Design.

US Army Corps of Engineers, 1957b. Design of Structures to Resist the Effects of Atomic Weapons – Principals of Structural Elements Subjected to Dynamic Loads.

US Navy, 1990. Structures to Resist the Effects of Accidental Explosions.

Wen, H. M., 1998. Deformation and tearing of clamped circular work-hardening plates under impulsive loading. Int. J. Pres. Ves. Pip. 75 (1), 67–73.

Yu, J., Jones, N., 1991. Further experimental investigations on the failure of clamped beams under impact loads. International Journal of Solids and Structures 27 (9), 1113 – 1137.
URL `http://www.sciencedirect.com/science/article/pii/002076839190114U`

Yu, T. X., Chen, F. L., 1992. The large deflection dynamic plastic response of rectangular plates. Int. J. Impact Eng. 12 (4), 605–616.

Yu, T. X., Chen, F. L., 1998. Failure modes and criteria of plastic structures under intense dynamic loading: a review. Met. Mater. 4 (3), 219–226.

Yuan, Y., Tan, P. J., 2013. Deformation and failure of rectangular plates subjected to impulsive loadings. Int. J. Impact Eng. 59, 46–59.

Yuan, Y., Tan, P. J., Li, Y., 2017. Dynamic structural response of laminated glass panels to blast loading. Comp. Struct. 182, 579–589.

Yuan, Y., Tan, P. J., Shojaei, K., Wrobel, P., 2016. Large deformation, damage evolution and failure of ductile structures to pulse-pressue loading. Int. J. Solids Struct. 96, 320–339.